1   **Geochronological and Geochemical Effects of Zircon Chemical Abrasion: Insights from Single-**
2   **Crystal Stepwise Dissolution Experiments**
3
4   **Alyssa J. McKanna[1], Blair Schoene[1], and Dawid Szymanowski[1,2]**
5
6   [1]Princeton University, Department of Geosciences, Princeton, New Jersey 08544, USA
7   [2]Institute of Geochemistry and Petrology, ETH Zurich, 8092 Zurich, Switzerland
8
9   **Correspondence:** Alyssa J. McKanna (ajmckanna@gmail.com)

10   **Abstract**

11   Chemical abrasion in hydrofluoric acid (HF) is routinely applied to zircon grains prior to U-Pb
12   dating by isotope dilution thermal ionization mass spectrometry (ID-TIMS) to remove radiation-
13   damaged portions of grains affected by Pb loss. Still, many chemically abraded datasets exhibit
14   evidence of residual Pb loss. Here we test how the temperature and duration of chemical
15   abrasion affects zircon U-Pb and trace element systematics in a series of 4-hour, single-crystal
16   stepwise dissolution experiments at 180 °C and 210 °C. Microtextural data for the zircon
17   samples studied is presented in a complementary paper by McKanna et al. (2023). We find that
18   stepwise dissolution at 210 °C is more effective at eliminating U, common Pb (Pb_c), and light
19   rare earth element (LREE) enriched material affected by open system behavior; reduces the
20   presence of leaching-induced artefacts that manifest as reverse discordance; and produces
21   more consistent and concordant results in zircon from the three rocks studied. We estimate
22   that stepwise dissolution in three 4 h steps is roughly equivalent to a single ~8 h leaching step
23   due to the insulating properties of the PTFE sleeve in the Parr pressure dissolution vessel,
24   whereas traditionally labs utilize a single 12-hour leaching step. We conclude that a single 8 h
25   leaching step at 210 °C should remove Pb-loss effects in the majority of zircon and that this can
26   be used as an effective approach for routine analysis. Further, we calculate time-integrated
27   alpha doses for leachates and residues from measured radionuclide concentrations to
28   investigate: 1) the alpha dose of the material dissolved at the two leaching conditions, and 2)
29   the apparent minimum alpha dose required for Pb loss susceptibility: $\geq 6 \times 10^{17}$ α/g.
30
31   **1. Introduction**

32   Zircon U-Pb geochronology by isotope dilution thermal ionization mass spectrometry (ID-TIMS)
33   has played a pivotal role in constraining the timing and tempo of processes on Earth from the
34   Hadean to the Pleistocene. Zircon is a remarkable chronometer, in part because crystalline
35   zircon is exceptionally chemically and physically durable. The zircon structure, however, can
36   accumulate radiation damage over time. Radiation damage is principally caused by alpha recoil
37   events in the ^{238}U, ^{235}U, and ^{232}Th decay series and the spontaneous fission of ^{238}U (Ewing et al.,
38   2003; Meldrum et al., 1998; Weber, 1990). Radiation-damaged zircon can lose Pb and less
39   commonly U, violating the basic requirement of geochronology that neither parent nor
40   daughter isotopes are lost through time except through radioactive decay (Geisler et al., 2002).
41   Fortunately, the dual $^{206}Pb/^{238}U$ and $^{207}Pb/^{235}U$ decay schemes provide a self-check mechanism

42 by which open system behavior can be identified in zircons older than several hundred Ma
43 (Mezger and Krogstad, 1997; Corfu, 2013). In the Phanerozoic, however, the dual decay system
44 becomes less effective at recognizing Pb loss, because the trajectory of Pb loss follows
45 concordia, and the precision of $^{207}Pb/^{235}U$ dates is also lower than corresponding $^{206}Pb/^{238}U$
46 dates due to the lower isotopic abundance of ^{235}U and consequently ^{207}Pb (Corfu, 2013;
47 Schoene, 2014).

48 In a seminal study, Mattinson (2005, 2011) – building off the previous findings of Krogh and
49 Davis (1975) and Todt and Büsch (1981) – demonstrated that the most radiation-damaged
50 portions of zircon can be effectively removed by hydrofluoric acid (HF) through a series of
51 stepwise dissolution experiments on multi-grain aliquots. He showed that early leaching steps
52 sampled high-U material with discordant U-Pb dates, while later leaching steps sampled low-U
53 residues unaffected by open-system behavior. Mattinson (2005, 2011) further established that
54 partially annealing zircon samples prior to leaching helps to minimize the unwanted elemental
55 and isotopic fractionation effects that plagued earlier leaching attempts (Davis and Krogh,
56 2000; Todt & Büsch, 1981). These experimental findings revolutionized the field of zircon U-Pb
57 geochronology by allowing scientists to attain meaningful geochronological results from zircon
58 affected by open-system behavior. Air abrasion – the pre-treatment technique previously used
59 to improve U-Pb concordance by removing crystal rims that tend to be more enriched in U and
60 exposed to alteration (Krogh, 1981) – was largely abandoned. Today, a variation of Mattinson's
61 approach – termed chemical abrasion – is applied to virtually all zircon grains prior to ID-TIMS
62 U-Pb isotopic analysis. In this variation, zircon crystals are annealed at 800 °C to 1200 °C for 36
63 h to 60 h and then leached in concentrated HF at 180 °C to 210 °C for 10 h to 18 h prior to
64 dissolution and isotopic analysis (Mundil et al., 2004; Huyskens et al., 2016; Widmann et al.,
65 2019).

66 The decrease in sample size from multi-grain aliquots to portions of single crystals and the
67 concurrent increase in analytical precision in TIMS over the past half-century (e.g., Schoene,
68 2014) demands a critical re-evaluation of the chemical abrasion technique and the accuracy of
69 the U-Pb ages that the Earth science community has come to rely on. Many studies have now
70 shown that chemically abraded zircon samples often still exhibit residual Pb loss. This challenge
71 is widely recognized in the ID-TIMS U-Pb community and has prompted investigations into the
72 effects of different annealing and leaching conditions on geochronological outcomes (Huyskens
73 et al., 2016; Widmann et al., 2019) and the microstructure of chemically abraded zircon
74 (McKanna et al., 2023), as well as new statistical approaches for evaluating over-dispersed U-Pb
75 datasets (Keller, 2023).

76 We build on the earlier work of Mattinson (2005, 2011) and present a series of new stepwise
77 dissolution experiments performed at the single-crystal scale. We evaluate the effects of
78 stepwise chemical abrasion at 180 °C and 210 °C on zircon U-Pb and trace element systematics
79 in three zircon samples – AS3, SAM-47, and KR18-04 – which span a range of crystallization
80 ages, geological settings, and radiation damage densities. These zircons come from the same
81 sample aliquots as studied by McKanna et al. (2023) in their recent microstructural

82 investigation of zircon dissolution, which presents a unique opportunity to integrate zircon
83 microtextures, geochronology, and geochemistry.

84 **2. Methods**

85

86 Zircon samples were annealed in quartz crucibles at 900 °C for 48 h in air in a box furnace prior
87 to the start of the experiments. Annealed grains were mounted in epoxy, polished, and imaged
88 by cathodoluminescence (CL) or backscattered electron (BSE) imaging using a XL30 FEG
89 scanning electron microscope equipped with a mini-Gatan CL detector and a semiconductor
90 BSE detector housed at the PRISM Imaging and Analysis Center at Princeton University. Images
91 of dated zircon crystals are presented in Fig. S1, Fig. S2, and Fig. S3.

92

93 The stepwise partial dissolution protocol outlined here is very similar to that of Keller et al.,
94 (2019, their Fig. 1). Crystals were plucked from epoxy mounts, rinsed in 30% HNO_3, and
95 individually transferred to 200 μL PFA microcapsules for partial dissolution in ~100 μL of
96 concentrated HF. Microcapsules were loaded into a PTFE-lined Parr pressure dissolution vessel
97 with 5 mL moat HF and placed in a box oven set to 180 °C or 210 °C for a period of 4 h. At the 4
98 h mark, the pressure vessel was removed from the oven and placed in front of a fan to cool to
99 room temperature.

100

101 The microcapsules were then removed from the pressure vessel and the leachate (the dissolved
102 zircon-HF mixture) from each microcapsule was transferred to a clean 7 mL PFA beaker using a
103 pipette. A fresh, acid-cleaned pipette tip was used for each sample transfer. Approximately 100
104 μL of 6N HCl was added to the residue (the remaining undissolved zircon) in the microcapsule,
105 and the microcapsule was capped and placed on the hotplate for 1 h. The 6N HCl was then
106 pipetted off the residue and added to the 7 mL PFA beaker with the sample leachate. The
107 residue was then sequentially rinsed in the microcapsule using a pipette with 3N HCl, 6N HCl,
108 30 % HNO_3, and concentrated HF. These rinses were discarded. About 100 μL of fresh
109 concentrated HF was then added to each residue for the second round of step leaching. In total,
110 samples were partially dissolved in a series of three 4-h leaching steps generating a L1, L2, and
111 L3 leachate for each zircon crystal.

112

113 After the L3 leachate was collected, the residue was again rinsed with acid and ~100 μL of fresh
114 HF was added to the microcapsule. Each residue was spiked with the EARTHTIME [205]Pb-[233]U-
115 [235]U tracer (Condon et al., 2015; McLean et al., 2015) and dissolved in a Parr pressure
116 dissolution vessel in a box oven at 210 °C for 48 h to 60 h. Each leachate was spiked with the
117 same tracer, capped, and placed on the hot plate for the same duration. Both leachates and
118 residues were then dried down on the hot plate. Residues were redissolved in ~100 μL of 6N
119 HCl in the Parr pressure vessel in the box oven at 180 °C overnight, and leachates were
120 redissolved in ~100 μL of 6N HCl on an 80 °C hot plate overnight. Afterward, all residues and
121 leachates were dried down on the hot plate and redissolved in 3N HCl in preparation for ion
122 exchange chromatography. This procedure was modified slightly for half of the KR18-04 zircon
123 samples treated at 210 °C to evaluate whether the incomplete dissolution of fluoride salts was
124 causing unwanted U-Pb elemental fractionation effects. For these samples, after each HF

125 leachate was collected, zircon residues were dried down completely on the hot plate before the
126 addition of ~100 μL of 6N HCl. Microcaps were then transferred back to the Parr pressure vessel
127 and redissolved at 180 °C overnight in the box oven. The 6N HCl liquid was then pipetted off the
128 residue and added to the sample's HF leachate in the 7 mL PFA beaker. This procedure was
129 repeated for the L2 and L3 leachates. All other steps remained the same.
130
131 PTFE columns were prepared with 50 μL of Eichrom AG1-X8 anion exchange resin, cleaned, and
132 equilibrated. Ion exchange chemistry for U and Pb followed the protocol established by Krogh
133 (1973) and modified by Schoene et al. (2010) for the collection of trace elements. Combined U
134 and Pb fractions were dried down with trace 0.05 M H_3PO_4 and loaded onto a zone-refined
135 rhenium filament with a silica gel emitter (Gerstenberger and Haase, 1997) for isotopic analysis
136 on one of the two IsotopX Phoenix TIMS at Princeton University. Lead isotopes were measured
137 on either the Daly/photomultiplier detector or ATONA Faraday system (Szymanowski and
138 Schoene, 2020), and U isotopes were measured as oxides on Faraday cups with 10^{12} Ω resistors
139 or on the ATONA Faraday system. Mass fractionation of Pb isotopic analyses was corrected for
140 with factors specific to each detector system, derived from a compilation of in-run values
141 measured in samples spiked with the EARTHTIME ^{202}Pb-^{205}Pb-^{233}U-^{235}U tracer using the known
142 ^{202}Pb/^{205}Pb ratio of the tracer. Mass fractionation of U isotopic analyses was corrected using the
143 known ^{233}U/^{235}U ratio of the tracer. Tripoli and ET-Redux software (Bowring et al., 2011;
144 McLean et al., 2011) were used for processing isotopic data and error propagation, assuming a
145 sample ^{238}U/^{235}U ratio of 137.818 ± 0.045 (2σ) (Heiss et al., 2012). All reported ^{206}Pb /^{238}U and
146 ^{207}Pb/^{206}Pb dates are calculated using the decay constants of Jaffey et al., (1971) and Th-
147 corrected assuming a magma Th/U ratio of 3.5. Reported uncertainties reflect 2σ analytical
148 uncertainties. Common Pb corrections assume a composition equivalent to the blank.
149
150 Major and trace element analyses were made using a Thermo Scientific iCap-Q inductively
151 coupled plasma mass spectrometer (ICPMS) at Princeton University following the procedure
152 developed by Schoene et al. (2010), with analytical parameters described in O'Connor et al.
153 (2022). Uranium concentrations were calculated from Th concentrations measured by ICPMS
154 and the Th/U ratio estimated from radiogenic ^{208}Pb and the ^{206}Pb/^{238}U age assuming
155 concordance between the U-Pb and Th-Pb systems.
156
157 **3. Geologic setting, sample description, and previous geochronology**
158
159 **3.1. AS3**
160
161 AS3 zircons are from an anorthosite from the Duluth Complex of northern Minnesota, USA that
162 formed during the Mesoproterozoic North American Midcontinent Rift (46°45'43.4" N,
163 92°09'32.4" W) (Paces & Miller, 1993; Miller et al., 2002; Schmitz et al., 2003; Swanson-Hysell
164 et al., 2019, 2020). The Duluth Complex is a massive layered mafic intrusion. The anorthositic
165 and layered series of the complex were emplaced at ~1096 Ma over a duration <1 m.y.
166 (Swanson-Hysell et al., 2020). The voluminous magmatism that formed the Duluth Complex is
167 attributed to decompression melting due to lithospheric extension occurring atop an upwelling
168 mantle plume (Swanson-Hysell et al., 2020). Rifting in the region ceased at ~1084 Ma (Swanson-

169   Hysell et al., 2019). Thermochronology data from the Minnesota River Valley in southern
170   Minnesota suggest that rocks in the region have sat at near-surface temperature conditions
171   since the Neoproterozoic (Guenthner et al., 2013; McDannell et al., 2022).
172
173   The AS3 sample studied is the same as that of Takehara et al. (2018). The rock sample is
174   composed of plagioclase, amphibole, clinopyroxene, and ilmenite with minor K-feldspar,
175   apatite, zircon, and baddeleyite. Partially chloritized amphiboles, altered plagioclase, and
176   zeolite veins indicate that this sample of AS3 has interacted with low-temperature
177   hydrothermal fluids as previously described (Takehara et al., 2018). Zircon grains are large
178   (>~200 μm) and occur as orange-to-orangish brown tabular prisms or anhedral shards. Grains
179   are fractured and often have melt inclusions elongated parallel to the *c*-axis. Crystals exhibit
180   concentric and convolute zonation patterns, and many grains are hydrothermally altered (Fig.
181   S1) (McKanna et al., 2023; Takehara et al., 2018). Altered grains and grains with inclusions were
182   included in the experiments to evaluate how well geochemical data traces the dissolution of
183   inclusions and altered material. Raman data indicate that grains have accumulated high
184   radiation damage densities with equivalent alpha doses of 2×10^{17} α/g to $>1\times10^{19}$ α/g with
185   significant intracrystalline variations in radiation damage (McKanna et al., 2023).
186
187   Paces and Miller (1993) presented the first U-Pb geochronological data for AS3 zircon. These
188   authors found that six multi-grain aliquots of air-abraded zircon crystals produced concordant
189   ID-TIMS U-Pb dates and assigned the sample a weighted-mean $^{207}Pb/^{206}Pb$ age of 1099.1 ± 0.5
190   Ma (2σ). Schmitz et al. (2003) later conducted additional ID-TIMS U-Pb isotopic analysis on
191   individual air-abraded AS3 zircon. The authors found that several crystals produced discordant
192   dates affected by recent Pb loss. Twelve concordant analyses yielded a concordia age of 1099.1
193   ± 0.2 Ma (2σ). Eight grains from the same sample were later analyzed by chemical abrasion ID-
194   TIMS by Schoene et al. (2006). The authors annealed grains at 900 °C for 60 h and chemically
195   abraded them in an $HF-HNO_3$ mixture at 180 °C for 12 h to 14 h. Residues produced concordant
196   dates with weighted mean $^{206}Pb/^{238}U$ and $^{207}Pb/^{206}Pb$ ages of 1095.9 ± 0.2 Ma and 1098.6 ± 0.3
197   Ma (2σ) assuming a zircon $^{238}U/^{235}U$ ratio of 137.88. Recalculating from published isotope ratios
198   (Schoene et al., 2006) and assuming an updated zircon $^{238}U/^{235}U$ of 137.818 ± 0.045 (2σ) (Heiss
199   et al., 2012) in the age equation yields a $^{207}Pb/^{206}Pb$ age of 1097.7 ± 0.3 (2σ). Age differences
200   between these and previous results were attributed by the authors to differences in tracer
201   calibration, which had been redone as part of Schoene et al. (2006). Takehara et al., (2018) later
202   demonstrated that zircons from a different sample of AS3 collected from the same sample
203   locality are strongly affected by alteration; sensitive high-resolution ion microprobe (SHRIMP)
204   analyses showed that altered zones yielded normally discordant U-Pb analyses; were enriched
205   in incompatible trace elements including LREEs, Ca, Mn, Fe, Al, Li, and K; and depleted in Zr and
206   Si.

207   3.2 SAM-47

208   SAM-47 is an Archean (~3.32 - 3.29 Ga) granodiorite from the Corunna Downs Granitic Complex
209   of the Emu Pools Supersuite in the eastern Pilbara Craton (21°24'29.01" S, 119°46'21.03" E)
210   (Barley and Pickard, 1999; Smithies et al., 2003; Van Kranendonk et al., 2007). The tectonic

211 significance of the dome and keel structures of the eastern Pilbara Craton are a matter of
212 debate (stagnate lid versus mobile lid tectonics), and the region has experienced a multi-phase
213 deformational history (Kloppenburg et al., 2001; MacLennan, 2019; Moore and Webb, 2013).
214 ID-TIMS U-Pb ages for apatite from the Corunna Downs Granitic Complex are ~3.3 Ga, which
215 are similar to Ar-Ar ages reported by Kloppenburg (2003). The similarity between the U-Pb and
216 Ar-Ar data suggest rapid cooling through ~460 °C following intrusion of the granitoid
217 (MacLennan, 2019). Zircon (U-Th)/He dates for the Owen's Gully diorite from the Mount Edgar
218 Granitic Complex north of the Corunna Downs range from 677.5 ± 36.3 Ma to 815.5 ± 44.6 Ma,
219 suggesting that the eastern craton reached near-surface thermal conditions, where radiation
220 damage can accumulate in zircon, sometime in the Neoproterozoic (Magee et al., 2017). Low-
221 temperature thermochronology data from elsewhere in the Pilbara craton (the northern,
222 central, and western blocks) suggest that the onset of widespread cooling related to basin-
223 development and unroofing varied regionally starting sometime between ~600 and 300 Ma
224 (Morón et al., 2020). Zircon grains separated from SAM-47 are euhedral, brown, translucent,
225 and finely-fractured (Fig. S2). Crystals display fine-scale concentric growth zones, and rims are
226 enriched in actinides and radiation damage relative to cores (McKanna et al., 2023). Raman
227 data suggest that grains have accumulated intermediate-to-high radiation damage densities
228 with equivalent alpha doses ranging from 6×10^{17} α/g to 2×10^{18} α/g (McKanna et al., 2023).
229 There is no previous zircon U-Pb geochronology from this sample, however, Pb loss is common
230 in similarly aged zircon from the Pilbara craton (MacLennan, 2019).

3.3 KR18-04

233 KR18-04 zircons come from a Neoproterozoic rhyolite body associated with the glaciolacustrine
234 Konnarock Formation in the Blue Ridge Mountains of Virginia, USA (MacLennan et al., 2020)
235 (36°41'47.95" N, 81°24'22.08" W). The Konnarock Formation is part of a structurally continuous
236 sedimentary sequence deposited in a continental rift environment (Merschat et al., 2014). This
237 sequence unconformably overlies gneisses that are related to the Mesoproterozoic Grenville
238 orogeny. ID-TIMS U-Pb ages for zircon separated from KR18-04 were used to show that glacial
239 sedimentation was occurring at tropical latitudes at ~751 Ma, 30 million years prior to the
240 Sturtian Snowball Earth (MacLennan et al., 2020). The post-depositional history of the region is
241 complex and poorly resolved (Roden, 1991). Zircon fission track dates ($T_{closure}$ = ~205 °C) from
242 the Blue Ridge are variably reset by burial reheating and range in age from ~617 Ma to late
243 Paleozoic dates (Naeser et al., 2016). Zircon (U-Th)/He dates ($T_{closure}$ = ~180 °C for crystalline
244 zircon) from the Blue Ridge are contemporaneous with the late-stages of the Alleghenian
245 orogeny indicating that the zircon He chronometer was fully reset by burial reheating and
246 records synorogenic exhumation (Basler et al., 2021).

248 The KR18-04 rhyolite is crystal-rich with prominent, dominantly euhedral K-feldspar and quartz
249 phenocrysts (MacLennan et al., 2020). Zircon grains separated from KR18-04 are euhedral, pink-
250 orange, transparent, and have few to no inclusions. Grains exhibit concentric zoning in
251 cathodoluminescence images with some faint, broad growth zones (Fig. S3). Raman data
252 suggest that grains have accumulated low-to-intermediate radiation damage densities with
253 equivalent alpha doses ranging from 5×10^{16} α/g to 2×10^{17} α/g (McKanna et al., 2023).

254 Twelve single-crystal zircon ID-TIMS U-Pb analyses for KR18-04 are presented by MacLennan et
255 al. (2020). Zircon grains were initially chemically abraded at 185 °C for 12 h. However, because
256 many of these analyses retained significant Pb loss, the intensity of chemical abrasion was
257 increased to 210 °C for up to 14 h for the remaining samples. The twelve reported $^{206}Pb/^{238}U$
258 dates – which combine both leaching conditions – range from 753.08 ± 0.33 Ma to 741.21 ±
259 0.35 Ma. The reported data are statistically over-dispersed for a single population. The authors
260 attribute the spread in ages along concordia and the one discordant analysis to residual Pb loss
261 (their Fig. S10). The reported eruption age for the sample derived from the eight oldest
262 analyses and determined using a Bayesian Markov Chain Monte Carlo technique is 752.60
263 +0.12/-0.65 Ma.
264
265 **4. Results**
266
267 **4.1 U-Pb geochronology**
268
269 **4.1.1 AS3**
270
271 L1 leachates are strongly affected by Pb loss and enriched in Pb_c derived from inclusions and
272 altered zones (Fig. 1, Table S1). L1 leachates either overlap the concordia curve due to large
273 uncertainties or are normally discordant. L2 and L3 leachates are older than L1 leachates and
274 form a discordia line of analyses that are either normally discordant, concordant, or reversely
275 discordant. The lower intercept ages of the discordia lines are zero-age. L2 and L3 leachates
276 treated at 180 °C are more enriched in Pb_c and ages are more widely dispersed compared to L2
277 and L3 leachates treated at 210 °C.
278
279 Residues treated at 210 °C form a single, concordant age population with a weighted mean
280 $^{206}Pb/^{238}U$ age of 1096.42 ± 0.49 Ma (MSWD = 1.7; Fig. 1). U-Pb ages of residues treated at 180
281 °C are dispersed along concordia and include reversely discordant analyses, although a cluster
282 of residue analyses yield a weighted mean $^{206}Pb/^{238}U$ age of 1096.29 ± 0.36 Ma (MSWD = 2.3) in
283 agreement with the 210 °C result. Weighted-mean $^{207}Pb/^{206}Pb$ ages for all leachates and
284 residues agree within uncertainty (Fig. 2). The weighted-mean $^{207}Pb/^{206}Pb$ ages obtained for
285 residues are 1097.03 ± 0.63 Ma (MSWD = 1.7) and 1096.64 ± 0.96 Ma (MSWD = 0.48), for the
286 180 °C and 210 °C datasets respectively. The new data agree well with previous geochronology
287 (Schoene et al., 2006).
288
289 **4.1.2 SAM-47**
290
291 L1 leachates from both sample sets are strongly affected by Pb loss (Fig. 3, Table S1). L2 and L3
292 leachates from the 180 °C experiment are also affected by significant Pb loss. In contrast, many
293 of the L2 and L3 leachates from the 210 °C experiment are concordant, and the few normally
294 discordant analyses closely approach concordia.
295
296 Residues from the 180 °C dataset form a discordia line with two concordant and four normally
297 discordant analyses. The two concordant residues have a weighted-mean $^{206}Pb/^{238}U$ age of

298 3319.5 ± 1.4 Ma (MSWD = 1.7). All 210 °C residues overlap or plot closely to concordia; three
299 concordant residues yield a weighted-mean $^{206}Pb/^{238}U$ age of 3316.1 ± 1.6 Ma (MSWD = 1.0).
300 Upper intercept ages for residues and 210 °C L2 and L3 leachates agree within uncertainty and
301 produce robust MSWDs (Fig. 3). The most precise upper and lower intercept ages are 3321.23
302 +0.78/-0.71 Ma and 751 ± 140 Ma, respectively. Most $^{207}Pb/^{206}Pb$ dates for L2, L3, and residue
303 samples from the 210 °C experiment agree within uncertainty (Fig. 2). 210 °C residues yield a
304 weighted-mean $^{207}Pb/^{206}Pb$ age of 3321.75 ± 0.63 Ma (MSWD = 0.83) in agreement with upper
305 intercept ages. In contrast, $^{207}Pb/^{206}Pb$ dates from the 180 °C dataset are notably younger,
306 indicating the dissolution of domains affected by ancient Pb loss. The two concordant 180 °C
307 residue analyses yield a weighted-mean $^{207}Pb/^{206}Pb$ age of 3320.90 ± 0.87 Ma (MSWD = 0.050).
308
309 **4.1.3 KR18-04**
310
311 L1 leachates from both sample sets are affected by Pb loss that occurred at zero-age (Fig. 4,
312 Table S1). L2 leachates from both experiments are concordant and older than zircon residues.
313 L3 leachates are generally concordant, younger than L2 leachates, and slightly older or within
314 uncertainty of zircon residues. Residues from the 180 °C experiment spread along concordia
315 from 758.63 Ma to 752.99 Ma. In contrast, residues from the 210 °C experiment form a tight
316 cluster with a weighted mean $^{206}Pb/^{238}U$ age of 752.49 ± 0.24 Ma (MSWD = 1.1, n=6) in
317 agreement with previous geochronology (MacLennan et al., 2020). This weighted-mean age
318 includes analyses measured on the ATONA, which produced more precise U measurements; the
319 batch of samples ran using the traditional amplifiers had very poor U ionization resulting in low
320 quality U measurements. The two 210 °C zircon aliquots that followed slightly different step-
321 leaching protocols as outlined in Methods generated equivalent results.
322
323 **4.2 Trace element geochemistry**
324
325 Major and trace element geochemistry data for AS3, SAM-47, and KR18-04 are reported in
326 Table S2. In the 180 °C experiments, leachates for the three zircon samples are enriched in LREE
327 and Pb_c relative to zircon residues (Fig. 5, Fig. 6, and Fig. 7). LREE enrichment is apparent both
328 in chondrite-normalized REE spider diagrams (Fig. S4, Fig. S5, and Fig. S6) and in LREE-indices
329 (LREE-I) (Table S3). LREE-indices – calculated as [Dy]/[Nd] + [Dy]/[Sm] following Bell et al.,
330 (2016) – quantify LREE-enrichment in zircon that reflects chemical alteration or sample
331 contamination. The lower the LREE-I, the higher the LREE-enrichment. In the 210 °C
332 experiments, L1 and some L2 leachates are enriched in LREE and Pb_c, but some L2 and all L3
333 leachates have LREE and $Pb*/Pb_c$ compositions similar to residues. Samples' LREE-I and
334 radiogenic to common Pb ratios ($Pb*/Pb_c$) are positively correlated.
335
336 AS3 leachates are enriched in U relative to residues in the 180 °C dataset (Fig. 8 and Table S3),
337 whereas in the 210 °C dataset only L1 leachates are U-enriched. A similar pattern is seen for
338 KR18-04: L1 and L2 leachates from the 180 °C dataset are enriched in U relative to residues, but
339 only L1 leachates are U-enriched in the 210 °C dataset. Results for SAM-47 differ. Some SAM-47
340 leachates are marginally enriched in U in the 180 °C dataset, while most leachates from the 210
341 °C experiment have U compositions similar to residues.

342   The percent zircon dissolved is calculated from measured Zr abundances: $(Zr_{step}/Zr_{total}) \times 100$
343   (Fig. 8 and Table S3). This calculation assumes that zircon residues fully dissolve during the final
344   digestion step. For AS3 samples, most dissolution occurred in L1 with progressively smaller
345   fractions dissolved in L2 and L3. The median fraction of the AS3 residue remaining in the 180 °C
346   and 210 °C experiments is ~55 % and ~30 %, respectively. For SAM-47 samples, only 10 % to 20
347   % of the zircon dissolved during leaching at 180 °C, leaving 80 % to 90 % of the zircon available
348   for final digestion. At 210 °C, most dissolution in SAM-47 samples occurred in L1 with
349   progressively smaller volumes dissolved in L2 and L3; zircon residues fractions are less than 40
350   %. For KR18-04 samples, only ~10 % to 15 % of zircon dissolved during leaching at 180 °C,
351   leaving residue fractions of ~85 % to 95 %. At 210 °C, ~10 % to 30 % of KR18-04 zircon dissolved
352   during leaching, resulting in 70 % to 90 % residue fractions. Percent Pb* $(Pb^*_{step}/Pb^*_{total} \times 100)$
353   calculations mirror results for percent zircon dissolved in all experiments (Fig. 8 and Table S3).
354
355   **5. Discussion**
356
357   **5.1 Reverse discordance**
358
359   Reverse discordance and concordant analyses that are older than the samples' interpreted
360   crystallization ages are common in the AS3 and KR18-04 datasets but absent in SAM-47.
361   Concordant analyses that are "too old" can result from either minor U loss or Pb* gain, causing
362   datasets to lie along a discordia line that overlies the concordia curve; for brevity, we will also
363   refer to these analyses as "reversely discordant." Reverse discordance is most common in L2
364   and L3 leachates, however, a subset of residues from the AS3 and KR18-04 180 °C datasets are
365   also reversely discordant. Three L2 leachates for the Hadean zircon analyzed by Keller et al.
366   (2019) are similarly reversely discordant.
367
368   Reverse discordance in zircon stepwise dissolution experiments is generally attributed to
369   leaching-induced experimental artefacts. Early step-leaching efforts yielded U-Pb isotopic
370   variations that swung wildly between normally and reversely discordant from step-to-step
371   (Todt and Büsch, 1981). Mattinson (1994, 2011) later attributed this effect to the authors'
372   specific dissolution and spiking method, which caused U and Pb to fractionate between
373   supernate and U-bearing fluoride precipitates. However, later step-leaching experiments using
374   different experimental procedures also exhibited reverse discordance in early leaching steps
375   (Chen et al., 2001; Mattinson, 2005, 2011). Mattinson (2005, 2011) charged that early leaching
376   steps must reflect a mixture of U and Pb from the dissolved zircon volume plus excess Pb*
377   leached from the intact zircon residue. Mattinson (2005, 2011) further demonstrated that
378   annealing samples at temperatures between 800 °C and 1100 °C prior to chemical abrasion
379   helped to minimize – but not eliminate – leaching-induced artefacts.
380
381   Reverse discordance is observed naturally in some untreated zircon (Kusiak et al., 2015;
382   Wiemer et al., 2017; Williams et al., 1984). In such cases, reverse discordance is generally
383   attributed to either the internal redistribution of Pb within a crystal or to external factors such
384   as alteration by hydrothermal fluids (Mattinson et al., 1996). Alpha recoil can displace Pb* from
385   the position of its parent radioisotope by ~30 nm (Ewing et al., 2003; Weber, 1990, 1993). In

386 crystals with fine-scale growth zoning, Pb* produced by a U atom within a high-U zone can be
387 implanted into a nearby low-U zone producing a localized occurrence of excess Pb* in the low-
388 U zone (Mattinson et al., 1996). Further, ion imaging and atom probe tomography studies of
389 zircon support the case for nano-to-micro scale Pb redistribution under elevated temperatures
390 and pressures (Kusiak et al., 2015; Peterman et al., 2019, 2021; Reddy et al., 2016). These
391 studies show that unsupported Pb* often forms clusters that are not spatially associated with
392 parent radionuclide growth patterns. However, the exact mechanisms by which Pb* migrates
393 through the zircon structure are poorly understood.
394
395 Notably, our SAM-47 zircon does not exhibit reverse discordance suggesting that only some
396 samples are predisposed to leaching-induced artifacts or leaching-exposed natural U-Pb
397 fractionation. A zircon's U-Pb systematics as revealed by stepwise dissolution must therefore
398 reflect its unique compositional characteristics such as the length-scale and magnitude of
399 radionuclide zonation, the extent of Pb loss, or the sample's geological history. AS3 is
400 hydrothermally altered, so a component of the reverse discordance observed could potentially
401 reflect the redistribution of Pb isotopes during hydrothermal alteration (Takehara et al., 2018).
402 Why KR18-04 zircon is susceptible to reverse discordance is less clear. Grains appear unaltered
403 and most compositional zones are broad; however, some grains do have thin, high-U zones that
404 could contribute to the internal redistribution of Pb* (McKanna et al., 2023 their Fig. 4 and
405 15a). Zircon fission track and (U-Th)/He data from Blue Ridge indicate that the region was
406 thermally affected by burial reheating during the late-Paleozoic Alleghenian Orogeny (Naeser et
407 al., 2016; Roden, 1991). Still, there is no evidence that KR18-04 has experienced an extreme
408 high-temperature deformation event. SAM-47 may lack leaching-induced reverse discordance
409 simply because Pb loss in the sample is so pervasive.
410
411 Regardless of the causes of reverse discordance, this work and that of Mattinson (2005, 2011)
412 demonstrate that increasing the leaching duration and/or temperature helps to eliminate
413 zircon domains affected by open system behavior. These results also highlight that under-
414 leaching samples can produce over-dispersed U-Pb datasets fraught with geologically
415 meaningless analyses. Without the additional context that the 210 °C experiment provides, a
416 researcher could easily interpret the older concordant dates from the 180 °C KR18-04 dataset,
417 for example, as inheritance or prolonged magmatic residence. We stress, however, that our
418 step-wise experiments are under-leached compared to the normal 12 h leaching step used in
419 most labs (see Section 4.3).
420
421 **5.2 The strengths and limitations of geochemical tools for identifying open-system behavior**
422
423 Common Pb and LREEs are incompatible in zircon. Mineral and melt inclusions and
424 hydrothermally altered or metamict zones, however, tend to be enriched in LREEs and common
425 Pb (Bell et al., 2016, 2019). Consequently, geochemical indicators such as a sample's LREE-index
426 (LREE-I = [Dy]/[Nd] + [Dy]/[Sm]) and Pb^*/Pb_c (provided demonstrably low laboratory blanks) are
427 useful tools for identifying contamination, hydrothermal alteration, and metamictization.
428 Indeed, our data show that the two variables are generally positively correlated (Fig. 5C, Fig. 6C,
429 and Fig. 7B). Another important geochemical indicator is U concentration – or effective U

430   concentration (eU = U + 0.235 × Th) – which is a measure of the relative radiation damage in a
431   sample.
432
433   These three geochemical indicators are useful tools for evaluating zircon dissolution. In the 180
434   °C experiments, L1, L2, and some L3 leachates are enriched in LREE, Pb_c, and U relative to zircon
435   residues. Whereas in the 210 °C experiments, L1 and some L2 leachates are enriched in the
436   three variables, however, some L2 and most L3 leachates have compositions similar to residues.
437
438   Micro-X-ray computed tomography data presented by McKanna et al. (2023) for AS3 and SAM-
439   47 zircon show that acid readily accesses crystal cores via fractures to dissolve mineral and melt
440   inclusions and strongly metamict zones during L1 at 180 °C and 210 °C. As such, we interpret
441   the LREE, Pb_c, and U enrichment in L1 leachates to reflect the dissolution of inclusions,
442   metamict material, and – in the case of AS3 – hydrothermally altered zones. We attribute LREE,
443   Pb_c, and U enrichments in later leaching steps to the continued dissolution of soluble radiation-
444   damaged or altered domains. KR18-04 zircon grains are more crystalline and typically lack
445   fractures. Consequently, acid only accesses the cores of some grains, and some inclusions
446   armored by highly crystalline material appear to survive twelve hours of chemical abrasion at
447   180 °C or 210 °C (McKanna et al., 2023). Consequently, LREE and Pb_c enrichment in L2 and L3
448   leaching steps could reflect later-stage dissolution of inclusions as well as the continued
449   dissolution of radiation-damaged or altered domains.
450
451   Comparing leachate and residue chemistry is extremely effective at illuminating the progress of
452   zircon dissolution. However, stepwise chemical abrasion is a time- and labor-intensive process.
453   The overwhelming majority of zircon ID-TIMS U-Pb studies perform single-step chemical
454   abrasion and discard the leachate; only the residue is characterized. In an ideal scenario,
455   geochemical indicators such as those described here could be used to support the inclusion or
456   exclusion of anomalously young (or old) analyses from geochronological interpretations. Fig. 9
457   shows ΔAge (Ma) of residues plotted as a function of a grain's LREE-I, Pb*/Pb_c, or eU. Delta-Age
458   is calculated as the difference between a residue's measured $^{206}Pb/^{238}U$ date and each sample's
459   accepted crystallization age. Negative values for ΔAge reflect Pb loss, while positive values
460   indicate reverse discordance.
461
462   Unfortunately, there is no clear correlation between either of the three geochemical indicators
463   and ΔAge in the samples analyzed. Instead, the data suggest that relative enrichments in LREE,
464   Pb_c, and U in residues are not reliable indicators of residual open system behavior. We
465   speculate that the residual zircon affected by open-system behavior is likely volumetrically
466   small compared to the volume of the residual closed-system zircon. Thus, the geochemical
467   signature of the open-system behavior is likely masked by the bulk chemistry of the closed-
468   system residue. Relative enrichments in LREE, Pb_c, and U in residues are likely useful
469   geochemical indicators only if the residual open-system material is proportionally large.
470
471   **5.3 Leaching temperature and one-step versus stepwise chemical abrasion**
472

473   Stepwise dissolution at 210 °C out-performed stepwise dissolution at 180 °C for all three zircon
474   samples and produced more consistent, concordant datasets. Leaching at 210 °C dissolved
475   zircon material affected by open-system behavior earlier in the leaching process minimizing the
476   frequency and magnitude of normal and reverse discordance compared to the 180 °C
477   experiments (Fig. 1, 2, 3, and 4). The efficacy of the higher leaching temperature is also evident
478   in zircon geochemistry; leaching at 210 °C more efficiently removed zircon material enriched in
479   U, LREE, and Pb_c.
480

481   Notably, U-Pb results for AS3 and KR18-04 residues treated by stepwise dissolution at 180 °C
482   are markedly worse than in previous studies (MacLennan et al., 2020; Schoene et al., 2006).
483   Chemical abrasion of AS3 zircon for 12 h to 14 h at 180 °C by Schoene et al. (2006) produced
484   concordant, statistically significant weighted mean U-Pb ages without signs of residual Pb loss
485   or reverse discordance. Those authors used intensive magnetic separation to target
486   diamagnetic zircon without inclusions, whereas this study included altered grains. While some
487   KR18-04 grains treated at 185 °C for 12 h by MacLennan et al., (2020) exhibited Pb loss, none of
488   their chemically abraded residues were found to be anomalously old or reversely discordant.
489

490   These apparent discrepancies beg the question: is stepwise dissolution in three 4 h leaching
491   steps equivalent to a single 12 h leaching step? PTFE has a low thermal conductivity making it
492   an effective insulator. To evaluate how temperature in the PTFE-lined Parr pressure dissolution
493   vessel changes with time, a small hole was drilled through the top of an old PTFE liner. The
494   pressure vessel was assembled as normal minus the rupture and corrosion disks. A type-K
495   thermocouple with an insulated wire was threaded through the top of the pressure vessel and
496   into the center of the PTFE liner. The pressure vessel was then placed in a box furnace at 180 °C
497   or 210 °C. Temperature was monitored using a Perfect Prime thermocouple until the
498   temperature in the liner reached equilibrium with the box furnace. The pressure vessel was
499   then removed from the furnace and placed in front of a fan, and temperature was recorded as
500   the pressure vessel cooled to room temperature.
501

502   Results indicate that PTFE is indeed a very effective insulator; the interior of the pressure vessel
503   heats and cools slowly (Fig. 10). It takes 90 min to 95 min for the interior of the pressure vessel
504   to reach within 20 °C of the target temperature and an additional 30 min to 35 min to reach
505   within 10 °C of the target temperature. The pressure vessel takes ~90 min to cool to room
506   temperature once removed from the oven.
507

508   Given the heating ramp up and cool down times for the PTFE-lined pressure dissolution vessel,
509   samples spend only ~2 h of a 4 h leaching step within 10 °C of the target temperature. As such,
510   a sample leached in three consecutive 4 h steps spends ~6 h within 10 °C of the target
511   temperature. Conversely, a sample leached in a single 12 h step spends ~10 h within 10 °C of
512   the target temperature – ~4 h longer than the step-leached sample. Volume loss estimates for
513   KR18-04 further support this conclusion; volume losses for crystals treated by stepwise
514   chemical abrasion (Fig. 8) are lower than volume losses for crystals chemically abraded in a
515   single 12-h step (McKanna et al., 2023; their Fig. 18).
516

517 We estimate that our dated residues have been leached for a duration equivalent to a single ~8
518 h leaching step on the basis of a 10 °C threshold. Given our U-Pb results, we conclude that
519 zircon chemically abraded at 180 °C for a single 8 h step are "undercooked" and will likely
520 produce data affected by residual Pb loss and/or leaching-induced artifacts. Unfortunately, we
521 cannot comment on the efficacy of the routinely practiced 12-h leaching at 180 ˚C used in many
522 labs, except to say it is likely more effective than the results for residues presented here. Zircon
523 samples chemically abraded at 210 °C for a single 8-h leach are likely to produce geologically
524 meaningful results.
525
526 **5.4 The relationships between alpha dose, Pb loss, and zircon dissolution: Moving toward a**
527 **more predictable model for chemical abrasion**
528
529 Zircon is an outstanding chronometer because radiogenic Pb is immobile in crystalline zircon
530 (Cherniak et al., 2009; Cherniak and Watson, 2000). Establishing the alpha dose at which
531 radiogenic Pb can mobilize within the zircon structure would help make Pb loss more
532 predictable. We calculate three different time-integrated alpha doses for each sample using Eq.
533 1 where N_A is Avogadro's number; ^{238}U, ^{235}U, and ^{232}Th are concentrations (ppm) determined
534 for leachates and residues; λ values are the respective decay constants; M values are the
535 respective molar masses (g/mol), and t is the chosen damage accumulation interval (Table 1
536 and Table S3).
537
538 Eq. 1
539 $$\alpha \text{ dose} = \frac{8 \cdot N_A \cdot {}^{238}U}{M_{238} \cdot 10^6} \cdot (e^{\lambda_{238}t} - 1) + \frac{7 \cdot N_A \cdot {}^{235}U}{M_{235} \cdot 10^6} \cdot (e^{\lambda_{235}t} - 1) + \frac{6 \cdot N_A \cdot {}^{232}Th}{M_{232} \cdot 10^6} \cdot (e^{\lambda_{232}t} - 1)$$
540
541 "Total" alpha dose assumes a damage accumulation interval equivalent to a sample's
542 crystallization age. This calculation ignores the possibility of radiation damage annealing.
543 "Present day" alpha dose estimates attempt to take geological annealing into account.
544 Radiation damage anneals at temperatures above ~200 °C to 300 °C on geological timescales
545 (Bernet, 2009; Yamada et al., 2007). The closure temperature for the (U-Th)/He system in
546 crystalline zircon is ~180 °C (Guenthner et al., 2013; Reiners et al., 2004). As such, we use
547 published zircon (U-Th)/He dates or thermal histories derived from zircon (U-Th)/He datasets
548 for the Minnesota River Valley (Guenthner et al., 2013; McDannell et al., 2022), the Eastern
549 Pilbara craton (Magee et al., 2017), and the Virginia Blue Ridge (Basler et al., 2021) to estimate
550 minimum damage accumulation intervals for samples' "present day" alpha doses. Because
551 zircon (U-Th)/He dates for the Eastern Pilbara craton broadly overlap the lower-intercept U-Pb
552 concordia age for SAM-47, we take the lower-intercept age as the damage accumulation
553 interval. Chosen intervals for "present day" alpha doses for AS3, SAM-47, and KR18-04 are 750
554 Ma, 751 Ma, and 298 Ma, respectively.
555
556 "Present day" alpha dose estimates can also be established independently using Raman
557 spectroscopy because key bands in the zircon Raman spectrum broaden predictably with
558 increasing alpha dose (Nasdala et al., 2001; Palenik et al., 2003). "Present day" alpha doses for
559 AS3 and SAM-47 closely match Raman-based alpha doses (α_r) determined by McKanna et al.

560   (2023) for zircon from the same sample aliquots (Table 1). "Present day" alpha doses for KR18-
561   04 have a similar lower bound but a higher upper bound compared to Raman estimates
562   (McKanna et al., 2023). Most likely, Raman measurements failed to capture volumetrically
563   small, higher-U domains such as the thin concentric dissolution features evident in secondary
564   electron images of KR18-04 residues (McKanna et al., 2023, their Fig. 15a-I reproduced here in
565   Fig. 13b).
566
567   The final calculation estimates alpha dose at the time of Pb loss. Because AS3 and KR18-04
568   exhibit zero-age Pb loss, "present day" and "Pb loss" alpha doses estimates are equivalent. The
569   Pb loss discord for SAM-47, however, suggests that Pb loss occurred in the distant geological
570   past at or before 751 ± 140 Ma (Fig. 3C). Therefore, the maximum "Pb loss" damage
571   accumulation interval is the difference between the sample's upper and lower intercept ages,
572   which equates to ~2571 Ma.
573
574   Fig. 11 shows the distribution of "Pb loss" alpha dose estimates for all leachates affected by Pb
575   loss. Despite vastly different geological settings and ranges in radiation damage densities,
576   leachates affected by Pb loss exhibit similar alpha dose distributions. The majority have alpha
577   doses that are $\geq 6 \times 10^{17}$ α/g. We therefore establish this alpha dose as our best estimate for
578   the threshold above which Pb can mobilize within the zircon structure. The mechanism that
579   mobilizes Pb – diffusion, leaching, or recrystallization – is not clear, however, fluids likely play
580   an important role. As such, while zircon with alpha doses above 6×10^{17} α/g may be *susceptible*
581   to Pb loss, not all damaged grains will be affected by open system behavior. Notably, the $6 \times$
582   10^{17} α/g threshold is somewhat lower than the alpha dose – 1×10^{18} α/g – at which zircon
583   material properties such as density begin to change (Ewing et al., 2003; Nasdala et al., 2004).
584   However, the 6×10^{17} α/g threshold is similar to some estimates for the alpha dose at which
585   helium diffusion begins to increase causing the closure temperature for He in zircon to decrease
586   (Anderson et al., 2017, 2020).
587   For the best geochronological outcomes, chemical abrasion should target zircon material
588   susceptible to Pb loss, i.e., material with alpha doses above 6×10^{17} α/g. Fig. 12 shows "present
589   day" alpha dose estimates for all leachates and residues from the 180 °C and 210 °C
590   experiments. The apparent differences in alpha dose between the two leaching temperatures
591   reflects the fraction of material dissolved in each step. At 180 °C, smaller volumes of high-U
592   zones dissolve, whereas at 210 °C larger volumes of material including both high-U and
593   medium-U zones dissolve causing average alpha doses to be lower in the 210 °C dataset.

594   In the 180 °C experiments, the median alpha dose decreases with increasing leaching duration
595   consistent with the expected effects of radiation damage on zircon solubility (Fig. 12). A
596   majority of residues from the 180 °C experiments have alpha doses $> 6 \times 10^{17}$ α/g suggesting
597   that residues may be affected by residual open system behavior in agreement with our U-Pb
598   isotopic results. Evidently, dissolving zircon with lower alpha doses requires longer leaching
599   durations at 180 °C than achieved in this study, which was equivalent to a single 8-h leach step.
600   In contrast, the median alpha dose for residues as well as L2 and L3 leachates from the 210 °C

601   experiments have alpha doses below the established threshold. Zircon material with alpha
602   doses ≥ 6 × 10^{17} α/g is thus readily dissolved at short leaching durations at 210 °C.

603   Framing Pb loss and zircon solubility in terms of alpha dose allows a user to better predict how
604   chemical abrasion might affect a specific zircon dataset. Chemical abrasion is a time-consuming
605   method that is applied to the majority of ID-TIMS U-Pb datasets, but it may be unnecessary for
606   low-alpha dose, inclusion-free zircon. Further, by estimating a sample's "present day" alpha
607   dose distribution, a user can better anticipate how a sample will dissolve (McKanna et al.,
608   2023). For example, if a sample has accumulated a lot of radiation damage like SAM-47,
609   leaching longer than a single 8-h step at 210 °C will likely leave little to no residue for isotopic
610   analysis. Whereas, if a sample has a lower average alpha dose like KR18-04, a longer 210 °C
611   leach is likely safe and potentially more effective.

613   Determining alpha dose prior to dissolution, however, remains an outstanding challenge.
614   Raman spectroscopy is one method that can be used to estimate alpha dose (Nasdala et al.,
615   2001; Palenik et al., 2003). Alpha dose can also be estimated from laser ablation ICPMS U-Pb
616   data, as laser ablation U-Pb analysis is often used for pre-screening grains for ID-TIMS U-Pb
617   dating. Unfortunately, both methods are time- and resource-intensive. Fig. 13 plots alpha dose
618   as a function of time for different U concentrations. As described above, different time intervals
619   can be selected for damage accumulation depending on the calculation's goal. This figure is a
620   simple visual representation that can help a researcher determine whether or not a sample is
621   likely to be susceptible to Pb loss given a range of possible U concentrations and a rough
622   estimate for the sample's damage accumulation interval.

624   As highlighted in Fig. 13b, perhaps the most persistent challenge when it comes to tailoring
625   chemical abrasion for a specific zircon dataset are crystal-specific factors such as the spatial
626   distribution and magnitude of intracrystalline variations in radiation damage, alteration,
627   inclusions, and fractures that strongly affect how a zircon dissolves as discussed in our
628   companion paper (McKanna et al., 2023). While micro-X-ray computed tomography can
629   visualize inclusions and fractures in zircon in three-dimensions (3D) (McKanna et al., 2023), at
630   present, no method exists for quantifying radiation damage zonation in 3D. Radionuclide zoning
631   explains the inconsistent dissolution behavior evidenced in Fig. 8. For example, the percent
632   zircon dissolved in each leaching step decreases from L1 to L3 for AS3 zircon, remains constant
633   or decreases for SAM-47 zircon, and remains constant or increases for KR18-04 zircon. This
634   inconsistent behavior occurs because the percent zircon dissolved is not only a function of
635   alpha dose, but also 1) the volumetric proportion of zircon with a given alpha dose, and 2)
636   which portions of a crystal are in contact with HF at any given time during the leaching process.
637   Building a comprehensive model for chemical abrasion will ultimately require both geochemical
638   and textural inputs.

640   **6. Conclusions**

642   Single-crystal stepwise dissolution experiments performed at 180 °C and 210°C provide new
643   insights into the geochronological and geochemical effects of chemical abrasion on zircon

644 datasets. Because of the insulating properties of the PTFE-lined pressure dissolution vessel,
645 stepwise dissolution in three 4-h leaching steps is not equivalent to a 12-h single-step chemical
646 abrasion, the method most commonly used by the zircon ID-TIMS U-Pb community. We
647 estimate that our stepwise dissolution approach is roughly equivalent to 8-h single-step
648 chemical abrasion. Stepwise dissolution at 180 °C produced over-dispersed U-Pb datasets
649 affected by both residual Pb loss and leaching-induced or leaching-exposed artefacts that
650 present as reverse discordance. Without the context of the 210 °C results, reverse discordance
651 in the 180 °C datasets could easily be mistaken for prolonged crystallization or inheritance and
652 lead to spurious geological interpretations. Longer leaching durations are likely needed to
653 produce robust geochronological datasets at 180 °C.

655 Stepwise dissolution at 210 °C outperformed the 180 °C experiments by all measures for the
656 three zircon samples analyzed producing more reproducible, concordant results. Ultimately,
657 how a zircon sample responds to any chemical abrasion protocol will be sample-dependent.
658 However, our results suggest that 8-h single-step chemical abrasion at 210 °C may be effective
659 at mitigating Pb loss and reverse discordance for a wide range of zircon samples. Further study
660 of different zircon samples is needed. Our results, however, clearly demonstrate that leaching
661 durations longer than an 8-h single step are required for chemical abrasion at 180 °C to be
662 effective.

664 Uranium or eU concentration, Pb*/Pb$_c$, and LREE enrichment are useful tools for tracking the
665 dissolution of inclusions and radiation-damaged or altered material during stepwise dissolution.
666 These geochemical indicators, however, are not effective at identifying residual Pb loss in the
667 zircon residues analyzed.

669 We attempted to constrain the relationship between Pb loss and radiation damage by
670 calculating an alpha dose for each leachate based on its measured radionuclide concentration
671 and an estimated damage accumulation interval informed by the sample's geologic history. "Pb
672 loss" alpha dose estimates suggest that Pb may mobilize within the zircon structure at alpha
673 doses as low as 6×10^{17} α/g. "Present day" alpha dose estimates indicate that many residues
674 treated by stepwise dissolution at 180 °C have alpha doses above the 6×10^{17} α/g threshold,
675 and consequently, many 180 °C residues are affected by residual Pb loss. The majority of
676 residues treated at 210 °C – and many L2 and L3 leachates – have "present day" alpha doses
677 below this threshold. Grains expected to have accumulated alpha doses < 6×10^{17} α/g based on
678 expected radionuclide concentrations and damage accumulation intervals are unlikely to be
679 affected by Pb loss and may not require chemical abrasion. However, chemical abrasion may
680 help improve the precision of U-Pb analyses even in low-damage grains by dissolving Pb$_c$-
681 bearing inclusions. The effectiveness of any chemical abrasion protocol will ultimately be
682 sample-dependent, because zircon dissolution depends not only on a grain's bulk chemistry,
683 but also the spatial distribution and magnitude of intracrystalline variations in radiation
684 damage.

685 **Data availability.** All data presented are included in this paper or the Supplement.

702   **References**
703
704   Anderson, A. J., Hodges, K. V., & van Soest, M. C. (2017). Empirical constraints on the effects of
705   radiation damage on helium diffusion in zircon. *Geochimica et Cosmochimica Acta*, *218*,
706   308–322. https://doi.org/10.1016/j.gca.2017.09.006
707   Anderson, A. J., van Soest, M. C., Hodges, K. V., & Hanchar, J. M. (2020). Helium diffusion in
708   zircon: Effects of anisotropy and radiation damage revealed by laser depth profiling.
709   *Geochimica et Cosmochimica Acta*, *274*, 45–62. https://doi.org/10.1016/j.gca.2020.01.049
710   Barley, M. E., & Pickard, A. L. (1999). 41-62 An extensive, crustally-derived. In *Precambrian
711   Research* (Vol. 96).
712   Basler, L. C., Baughman, J. S., Fame, M. L., & Haproff, P. J. (2021). Spatially variable syn- and
713   post-Alleghanian exhumation of the central Appalachian Mountains from zircon (U-Th)/He
714   thermochronology. *Geosphere*, *17*(4), 1151–1169. https://doi.org/10.1130/GES02368.1
715   Bell, E. A., Boehnke, P., Barboni, M., & Harrison, T. M. (2019). Tracking chemical alteration in
716   magmatic zircon using rare earth element abundances. *Chemical Geology*, *510*, 56–71.
717   https://doi.org/10.1016/j.chemgeo.2019.02.027
718   Bell, E. A., Boehnke, P., & Harrison, T. M. (2016). Recovering the primary geochemistry of Jack
719   Hills zircons through quantitative estimates of chemical alteration. *Geochimica et
720   Cosmochimica Acta*, *191*, 187–202. https://doi.org/10.1016/j.gca.2016.07.016
721   Bernet, M. (2009). A field-based estimate of the zircon fission-track closure temperature.
722   *Chemical Geology*, *259*(3–4), 181–189. https://doi.org/10.1016/j.chemgeo.2008.10.043

723   Bowring, J. F., McLean, N. M., & Bowring, S. A. (2011). Engineering cyber infrastructure for U-Pb
724   geochronology: Tripoli and U-Pb-Redux. *Geochemistry, Geophysics, Geosystems*, *12*(6).
725   https://doi.org/10.1029/2010GC003479

726   Chen, F., Siebel, W., & Satir, M. (2001). Zircon U-Pb and Pb-isotope fractionation during
727   stepwise HF acid leaching and geochronological implications. In *Chem. Geol* (Vol. 172).
728   www.elsevier.com/locate/chemgeo

729   Cherniak, D. J., & Watson, E. B. (2000). Pb diffusion in zircon. *Chemical Geology*, *172*, 5–24.
730   www.elsevier.comrlocaterchemgeo

731   Cherniak, D. J., Watson, E. B., & Thomas, J. B. (2009). Diffusion of helium in zircon and apatite.
732   *Chemical Geology*, *268*(1–2), 155–166. https://doi.org/10.1016/j.chemgeo.2009.08.011

733   Condon, D. J., Schoene, B., McLean, N. M., Bowring, S. A., & Parrish, R. R. (2015). Metrology and
734   traceability of U-Pb isotope dilution geochronology (EARTHTIME Tracer Calibration Part I).
735   *Geochimica et Cosmochimica Acta*, *164*, 464–480.
736   https://doi.org/10.1016/j.gca.2015.05.026

737   Corfu, F. (2013). A century of U-pb geochronology: The long quest towards concordance. In
738   *Bulletin of the Geological Society of America* (Vol. 125, Issues 1–2, pp. 33–47).
739   https://doi.org/10.1130/B30698.1

740   Davis, D. W., & Krogh, T. E. (2000). Preferential dissolution of 234 U and radiogenic Pb from a-
741   recoil-damaged lattice sites in zircon: implications for thermal histories and Pb isotopic
742   fractionation in the near surface environment. In *Chemical Geology* (Vol. 172).
743   www.elsevier.comrlocaterchemgeo

744   Ewing, R. C., Meldrum, A., Wang, L., Weber, W. J., & Corrales, L. R. (2003). Radiation Effects in
745   Zircon. *Reviews in Mineralogy and Geochemistry*, *53*(1), 387–425.
746   https://doi.org/10.2113/0530387

747   Geisler, T., Pidgeon, R. T., van Bronswijk, W., & Kurtz, R. (2002). Transport of uranium, thorium,
748   and lead in metamict zircon under low-temperature hydrothermal conditions. *Chemical
749   Geology*, *191*, 141–154. www.elsevier.com/locate/chemgeo

750   Gerstenberger, H., & Haase, G. (1997). A highly effective emitter substance for mass
751   spectrometric Pb isotope ratio determinations. In *Chemical Geology* (Vol. 136).

752   Guenthner, W. R., Reiners, P. W., Ketcham, R. A., Nasdala, L., & Giester, G. (2013). Helium
753   diffusion in natural zircon: radiation damage, anisotropy, and the interpretation of zircon
754   (U-TH)/He thermochronology. *American Journal of Science*, *313*(3), 145–198.
755   https://doi.org/10.2475/03.2013.01

756   Heiss, J., Condon, D. J., McLean, N., & Noble, S. R. (2012). 238U/235U Systematics in Terrestrial
757   Uranium-Bearing Minerals. *Science*, *335*(6076), 1610–1613.

758   Huyskens, M. H., Zink, S., & Amelin, Y. (2016). Evaluation of temperature-time conditions for
759   the chemical abrasion treatment of single zircons for U-Pb geochronology. *Chemical
760   Geology*, *438*, 25–35. https://doi.org/10.1016/j.chemgeo.2016.05.013

761   Jaffey, A. H., Flynn, K. F., Glendenin, L. E., Bentley, W. C., & Essling, A. M. (1971). Precision
762   Measurement of Half-Lives and Specific Activities of 235U and 238U. *Physical Review C*,
763   *4*(5), 1889–1906. https://doi.org/10.1103/PhysRevC.4.1889

764   Keller, B. (2023). Technical Note: Pb loss-aware Eruption/Deposition Age Estimation. *GChron*,
765   *Preprint*. https://doi.org/10.5194/gchron-2023-9

766 Keller, B. C., Boehnke, P., Schoene, B., & Harrison, T. M. (2019). Stepwise chemical abrasion-
767   isotope dilution-thermal ionization mass spectrometry with trace element analysis of
768   microfractured Hadean zircon. *Geochronology*, *1*(1), 85–97.
769   https://doi.org/10.5194/gchron-1-85-2019
770 Kloppenburg, A. (2003). *Structural evolution of the Marble Bar Domain, Pilbara granite-*
771   *greenstone terrain, Australia : the role of Archaean mid-crustal detachments = Structurele*
772   *evolutie van het Marble Bar Domein, Pilbara graniet-groensteen terrein, Australie : de rol*
773   *van Archaeische decollements in de middenkorst* [PhD Dissertation]. Utrecht University.
774 Kloppenburg, A., White, S. H., & Zegers, T. E. (2001). Structural evolution of the Warrawoona
775   Greenstone Belt and adjoining granitoid complexes, Pilbara Craton, Australia: implications
776   for Archaean tectonic processes. In *Precambrian Research* (Vol. 112).
777   www.elsevier.com/locate/precamres
778 Krogh, T. E. (1973). A low-contamination method for hydrothermal decomposition of zircon and
779   extraction of U and Pb for isotopic age determinations. *Geochimica et Cosmochimica Acta*,
780   *37*, 485–494.
781 Krogh, T. E. (1981). Improved accuracy of U-Pb zircon ages by the creation of more concordant
782   systems using an air abrasion technique. *Geochimica et Cosmochimico Acta*, *46*, 637–649.
783 Kusiak, M. A., Dunkley, D. J., Wirth, R., Whitehouse, M. J., Wilde, S. A., & Marquardt, K. (2015).
784   Metallic lead nanospheres discovered in ancient zircons. *Proceedings of the National*
785   *Academy of Sciences of the United States of America*, *112*(16), 4958–4963.
786   https://doi.org/10.1073/pnas.1415264112
787 MacLennan, S. A. (2019). *Temporal constraints on Archean crustal geodynamics and*
788   *Neoproterozoic glaciation* [PhD Dissertation]. Princeton University.
789 MacLennan, S. A., Eddy, M. P., Merschat, A. J., Mehra, A. K., Crockford, P. W., Maloof, A. C.,
790   Southworth, C. S., & Schoene, B. (2020). Geologic evidence for an icehouse Earth before
791   the Sturtian global glaciation. *Science Advances*, *6*(24).
792   https://doi.org/10.1126/sciadv.aay6647
793 Magee, C. W., Danišík, M., & Mernagh, T. (2017). Extreme isotopologue disequilibrium in
794   molecular SIMS species during SHRIMP geochronology. *Geoscientific Instrumentation,*
795   *Methods and Data Systems*, *6*(2), 523–536. https://doi.org/10.5194/gi-6-523-2017
796 Mattinson, J. M. (1994). Mineralogy and Petrology A study of complex discordance in zircons
797   using step-wise dissolution techniques. *Contributions to Mineralogy and Petrology*, *116*,
798   117–129.
799 Mattinson, J. M. (2005). Zircon U-Pb chemical abrasion ("CA-TIMS") method: Combined
800   annealing and multi-step partial dissolution analysis for improved precision and accuracy
801   of zircon ages. *Chemical Geology*, *220*(1–2), 47–66.
802   https://doi.org/10.1016/j.chemgeo.2005.03.011
803 Mattinson, J. M. (2011). Extending the Krogh legacy: development of the CA–TIMS method for
804   zircon U–Pb geochronologyThis article is one of a series of papers published in this Special
805   Issue on the theme of *Geochronology* in honour of Tom Krogh. *Canadian Journal of Earth*
806   *Sciences*, *48*(2), 95–105. https://doi.org/10.1139/E10-023
807 Mattinson, J. M., Graubard, C. M., Parkinson, D. L., & McClelland, W. C. (1996). U-Pb Reverse
808   Discordance in Zircons: The Role of Fine-Scale Oscillatory Zoning and Sub-Micron Transport

809   of Pb. In A. Basu & S. Hart (Eds.), *Earth Processes: Reading the Isotopic Code* (pp. 355–370).
810   AGU. https://doi.org/10.1029/GM095p0355

811 McDannell, K. T., Keller, C. B., Guenthner, W. R., Zeitler, P. K., & Shuster, D. L. (2022).
812   Thermochronologic constraints on the origin of the Great Unconformity. *Proceedings of*
813   *the National Academy of Sciences*, *119*(5). https://doi.org/10.1073/pnas.2118682119

814 McKanna, A. J., Koran, I., Schoene, B., & Ketcham, R. A. (2023). Chemical abrasion: the
815   mechanics of zircon dissolution. *Geochronology*, *5*(1), 127–151.
816   https://doi.org/10.5194/gchron-5-127-2023

817 McLean, N. M., Bowring, J. F., & Bowring, S. A. (2011). An algorithm for U-Pb isotope dilution
818   data reduction and uncertainty propagation. *Geochemistry, Geophysics, Geosystems*,
819   *12*(6). https://doi.org/10.1029/2010GC003478

820 McLean, N. M., Condon, D. J., Schoene, B., & Bowring, S. A. (2015). Evaluating uncertainties in
821   the calibration of isotopic reference materials and multi-element isotopic tracers
822   (EARTHTIME Tracer Calibration Part II). *Geochimica et Cosmochimica Acta*, *164*, 481–501.
823   https://doi.org/10.1016/j.gca.2015.02.040

824 Meldrum, A., Boatner, L. A., Weber, W. J., & Ewing, R. C. (1998). Radiation damage in zircon and
825   monazite. *Geochimica et Cosmochimica Acta*, *62*(14), 2509–2520.

826 Merschat, A. J., Southworth, S., McClellan, E., Tollo, R. P., Rankin, D. W., Hooper, S., & Bauer, S.
827   (2014). Key structural and stratigraphic relationships from the northeast end of the
828   Mountain City window and the Mount Rogers area, Virginia–North Carolina–Tennessee. In
829   *Elevating Geoscience in the Southeastern United States: New Ideas about Old Terranes—*
830   *Field Guides for the GSA Southeastern Section Meeting, Blacksburg, Virginia, 2014* (pp. 63–
831   101). Geological Society of America. https://doi.org/10.1130/2014.0035(03)

832 Mezger, K., & Krogstad, E. J. (1997). Interpretation of discordant U-Pb zircon ages: An
833   evaluation. *Journal of Metamorphic Geology*, *15*(1), 127–140.
834   https://doi.org/10.1111/j.1525-1314.1997.00008.x

835 Miller, J. S., Matzel, J. E. P., Miller, C. F., Burgess, S. D., & Miller, R. B. (2007). Zircon growth and
836   recycling during the assembly of large, composite arc plutons. *Journal of Volcanology and*
837   *Geothermal Research*, *167*(1–4), 282–299.
838   https://doi.org/10.1016/j.jvolgeores.2007.04.019

839 Moore, W. B., & Webb, A. A. G. (2013). Heat-pipe Earth. *Nature*, *501*(7468), 501–505.
840   https://doi.org/10.1038/nature12473

841 Morón, S., Kohn, B. P., Beucher, R., Mackintosh, V., Cawood, P. A., Moresi, L., & Gallagher, S. J.
842   (2020). Denuding a Craton: Thermochronology Record of Phanerozoic Unroofing From the
843   Pilbara Craton, Australia. *Tectonics*, *39*(9). https://doi.org/10.1029/2019TC005988

844 Mundil, R., Ludwig, K. R., Metcalfe, I., & Renne, P. R. (2004). Age and Timing of the Permian
845   Mass Extinctions: U/Pb Dating of Closed-System Zircons. *Science*, *305*, 1760–1762.
846   www.sciencemag.org

847 Naeser, C. W., Naeser, N. D., Newell, W. L., Southworth, S., Edwards, L. E., & Weems, R. E.
848   (2016). Erosional and depositional history of the Atlantic passive margin as recorded in
849   detrital zircon fission-track ages and lithic detritus in Atlantic Coastal plain sediments.
850   *American Journal of Science*, *316*(2), 110–168. https://doi.org/10.2475/02.2016.02

851 Nasdala, L., Reiners, P. W., Garver, J. I., Kennedy, A. K., Stern, R. A., Balan, E., & Wirth, R. (2004).
852   Incomplete retention of radiation damage in zircon from Sri Lanka. *American Mineralogist*,
853   *89*, 219–231.
854 Nasdala, L., Wenzel, M., Vavra, G., Irmer, G., Wenzel, T., & Kober, B. (2001). Metamictisation of
855   natural zircon: Accumulaton versus thermal annealing of radioactivity-induced damage.
856   *Contributions to Mineralogy and Petrology*, *141*(2), 125–144.
857   https://doi.org/10.1007/s004100000235
858 O'Connor, L., Szymanowski, D., Eddy, M. P., Samperton, K. M., & Schoene, B. (2022). A red bole
859   zircon record of cryptic silicic volcanism in the Deccan Traps, India. *Geology*, *50*(4), 460–
860   464. https://doi.org/10.1130/G49613.1
861 Paces, J. B., & Miller, J. D. (1993). Precise U-Pb ages of Duluth Complex and related mafic
862   intrusions, northeastern Minnesota: geochronological insights to physical, petrogenetic,
863   paleomagnetic, and tectonomagmatic processes associated with the 1.1 Ga Midcontinent
864   Rift system. *Journal of Geophysical Research*, *98*(B8). https://doi.org/10.1029/93jb01159
865 Palenik, C. S., Nasdala, L., & Ewing, R. C. (2003). Radiation damage in zircon. *American*
866   *Mineralogist*, *88*, 770–781.
867 Peterman, E. M., Reddy, S. M., Saxey, D. W., Fougerouse, D., Snoeyenbos, D. R., & Rickard, W.
868   D. A. (2019). Nanoscale processes of trace element mobility in metamorphosed zircon.
869   *Contributions to Mineralogy and Petrology*, *174*(11). https://doi.org/10.1007/s00410-019-
870   1631-1
871 Peterman, E. M., Reddy, S. M., Saxey, D. W., Fougerouse, D., Zakaria Quadir, M., & Jercinovic,
872   M. J. (2021). Trace-element segregation to dislocation loops in experimentally heated
873   zircon. *American Mineralogist*, *106*(12), 1971–1979. https://doi.org/10.2138/am-2021-
874   7654
875 Reddy, S. M., van Riessen, A., Saxey, D. W., Johnson, T. E., Rickard, W. D. A., Fougerouse, D.,
876   Fischer, S., Prosa, T. J., Rice, K. P., Reinhard, D. A., Chen, Y., & Olson, D. (2016).
877   Mechanisms of deformation-induced trace element migration in zircon resolved by atom
878   probe and correlative microscopy. *Geochimica et Cosmochimica Acta*, *195*, 158–170.
879   https://doi.org/10.1016/j.gca.2016.09.019
880 Reiners, P. W., Spell, T. L., Nicolescu, S., & Zanetti, K. A. (2004). Zircon (U-Th)/He
881   thermochronometry: He diffusion and comparisons with 40Ar/39Ar dating. *Geochimica et*
882   *Cosmochimica Acta*, *68*(8), 1857–1887. https://doi.org/10.1016/j.gca.2003.10.021
883 Roden, M. K. (1991). Apatite Fission-Track Thermochronology of the Southern Appalachian
884   Basin: Maryland, West Virginia, and Virginia. *The Journal of Geology*, *99*(1), 41–53.
885   https://doi.org/10.1086/629472
886 Schmitz, M. D., Bowring, S. A., & Ireland, T. R. (2003). *Evaluation of Duluth Complex anorthositic*
887   *series (AS3) zircon as a U-Pb geochronological standard: New high-precision isotope*
888   *dilution thermal ionization mass spectrometry results*. https://doi.org/10.1016/S0016-
889   7037(00)00200-X
890 Schoene, B. (2014). U–Th–Pb Geochronology. In *Treatise on Geochemistry* (pp. 341–378).
891   Elsevier. https://doi.org/10.1016/B978-0-08-095975-7.00310-7
892 Schoene, B., Crowley, J. L., Condon, D. J., Schmitz, M. D., & Bowring, S. A. (2006). Reassessing
893   the uranium decay constants for geochronology using ID-TIMS U-Pb data. *Geochimica et*
894   *Cosmochimica Acta*, *70*(2), 426–445. https://doi.org/10.1016/j.gca.2005.09.007

895   Schoene, B., Latkoczy, C., Schaltegger, U., & Günther, D. (2010). A new method integrating high-
896   precision U-Pb geochronology with zircon trace element analysis (U-Pb TIMS-TEA).
897   *Geochimica et Cosmochimica Acta*, *74*(24), 7144–7159.
898   https://doi.org/10.1016/j.gca.2010.09.016
899   Smithies, R. H., Champion, D. C., & Cassidy, K. F. (2003). Formation of Earth's early Archaean
900   continental crust. *Precambrian Research*, *127*(1–3), 89–101.
901   https://doi.org/10.1016/S0301-9268(03)00182-7
902   Swanson-Hysell, N. L., Hoaglund, S. A., Crowley, J. L., Schmitz, M. D., Zhang, Y., & Miller, J. D.
903   (2020). Rapid emplacement of massive Duluth Complex intrusions within the North
904   American Midcontinent Rift. *Geology*, *49*(2), 185–189. https://doi.org/10.1130/G47873.1
905   Swanson-Hysell, N. L., Ramezani, J., Fairchild, L. M., & Rose, I. R. (2019). Failed rifting and fast
906   drifting: Midcontinent Rift development, Laurentia's rapid motion and the driver of
907   Grenvillian orogenesis. *Bulletin of the Geological Society of America*, *131*(5–6), 913–940.
908   https://doi.org/10.1130/B31944.1
909   Szymanowski, D., & Schoene, B. (2020). U–Pb ID-TIMS geochronology using ATONA amplifiers.
910   *Journal of Analytical Atomic Spectrometry*, *35*(6), 1207–1216.
911   https://doi.org/10.1039/D0JA00135J
912   Takehara, M., Horie, K., Hokada, T., & Kiyokawa, S. (2018). New insight into disturbance of U-Pb
913   and trace-element systems in hydrothermally altered zircon via SHRIMP analyses of zircon
914   from the Duluth Gabbro. *Chemical Geology*, *484*, 168–178.
915   https://doi.org/10.1016/j.chemgeo.2018.01.028
916   Todt, W. A., & Büsch, W. (1981). U-Pb investigations on zircons from pre-Variscan gneisses-I. A
917   study from the Schwarzwald, West Germany. *Geochimica et Cosmochimica Acta*, *45*, 1789–
918   1801.
919   Van Kranendonk, M. J., Hugh Smithies, R., Hickman, A. H., & Champion, D. C. (2007). Review:
920   Secular tectonic evolution of Archean continental crust: interplay between horizontal and
921   vertical processes in the formation of the Pilbara Craton, Australia. In *Terra Nova* (Vol. 19,
922   Issue 1, pp. 1–38). https://doi.org/10.1111/j.1365-3121.2006.00723.x
923   Weber, W. J. (1990). Radiation-induced defects and amorphization in zircon. *J. Mater. Res.*,
924   *5*(11), 2687–2697. http://journals.cambridge.org
925   Weber, W. J. (1993). Alpha-Decay-Induced Amorphization in Complex Silicate Structures.
926   *Journal of the American Ceramic Society*, *76*(7), 1729–1738.
927   https://doi.org/10.1111/j.1151-2916.1993.tb06641.x
928   Widmann, P., Davies, J. H. F. L., & Schaltegger, U. (2019). Calibrating chemical abrasion: Its
929   effects on zircon crystal structure, chemical composition and U–Pb age. *Chemical Geology*,
930   *511*, 1–10. https://doi.org/10.1016/j.chemgeo.2019.02.026
931   Wiemer, D., Allen, C. M., Murphy, D. T., & Kinaev, I. (2017). Effects of thermal annealing and
932   chemical abrasion on ca. 3.5 Ga metamict zircon and evidence for natural reverse
933   discordance: Insights for U[sbnd]Pb LA-ICP-MS dating. *Chemical Geology*, *466*, 285–302.
934   https://doi.org/10.1016/j.chemgeo.2017.06.019
935   Williams, I. S., Compston, W., Black, L. P., Ireland, T. R., & Foster, J. J. (1984). Contributions to
936   Mineralogy and Petrology Unsupported radiogenic Pb in zircon: a cause of anomalously
937   high Pb-Pb, U-Pb and Th-Pb ages. In *Contrib Mineral Petrol* (Vol. 88).

938   Yamada, R., Murakami, M., & Tagami, T. (2007). Statistical modelling of annealing kinetics
939   of fission tracks in zircon; Reassessment of laboratory experiments. *Chemical*
940   *Geology*, *236*(1–2), 75–91. https://doi.org/10.1016/j.chemgeo.2006.09.002
941
942
943
944
945
946
947
948
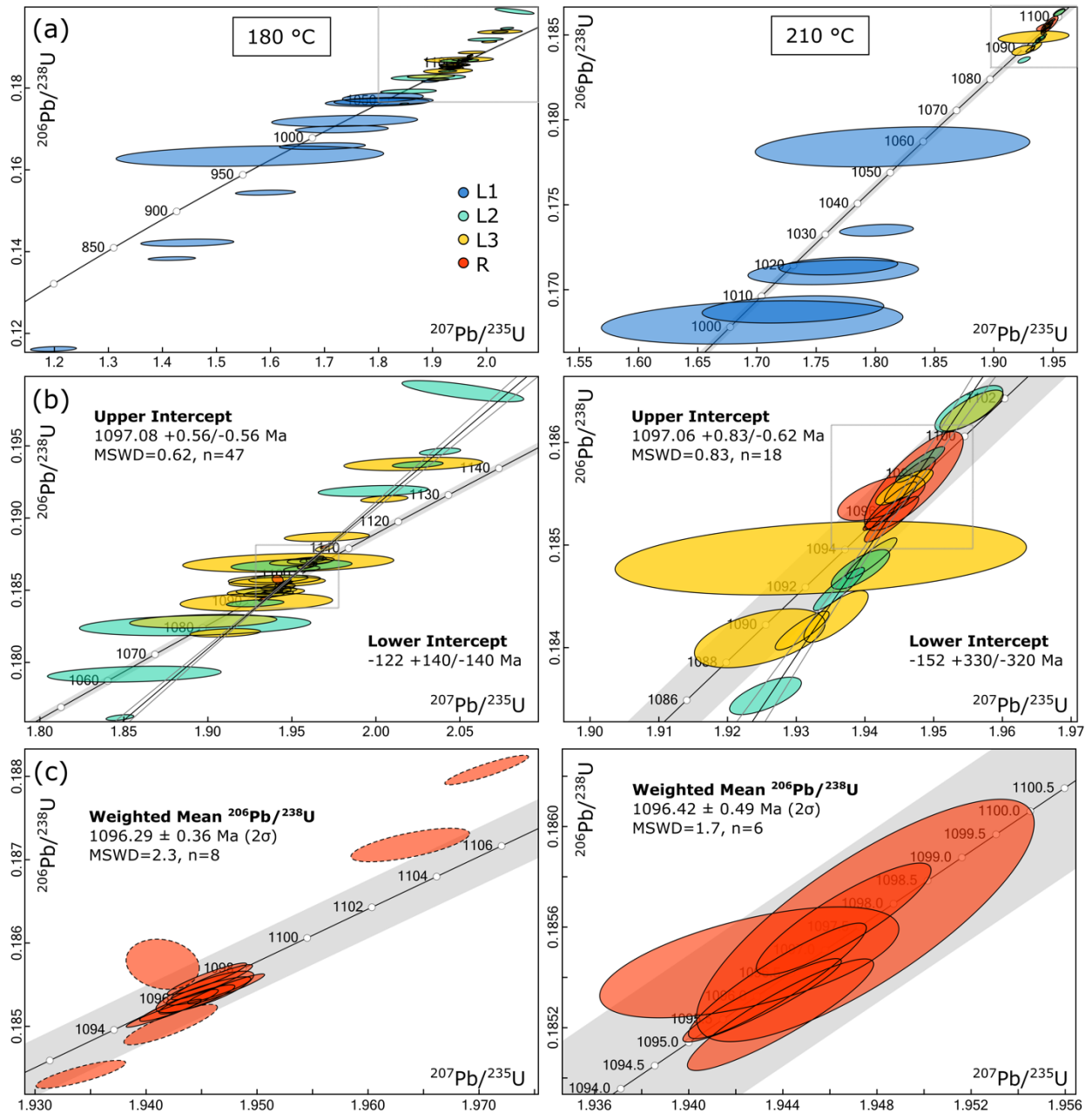
Figure 1. U-Pb concordia diagrams for the 180 °C (left) and 210 °C (right) AS3 experiments. **(a)** All data are depicted except for L1 leachates with Pb*/Pb$_c$ values < 1. **(b)** Close up of L2, L3, and R data. **(c)** Close up of zircon residue data. Ellipses with dashed borders were excluded from the weighted-mean ^{206}Pb/^{238}U age for the 180 °C experiment. All ellipses reflect 2σ analytical uncertainties.

949
950

24
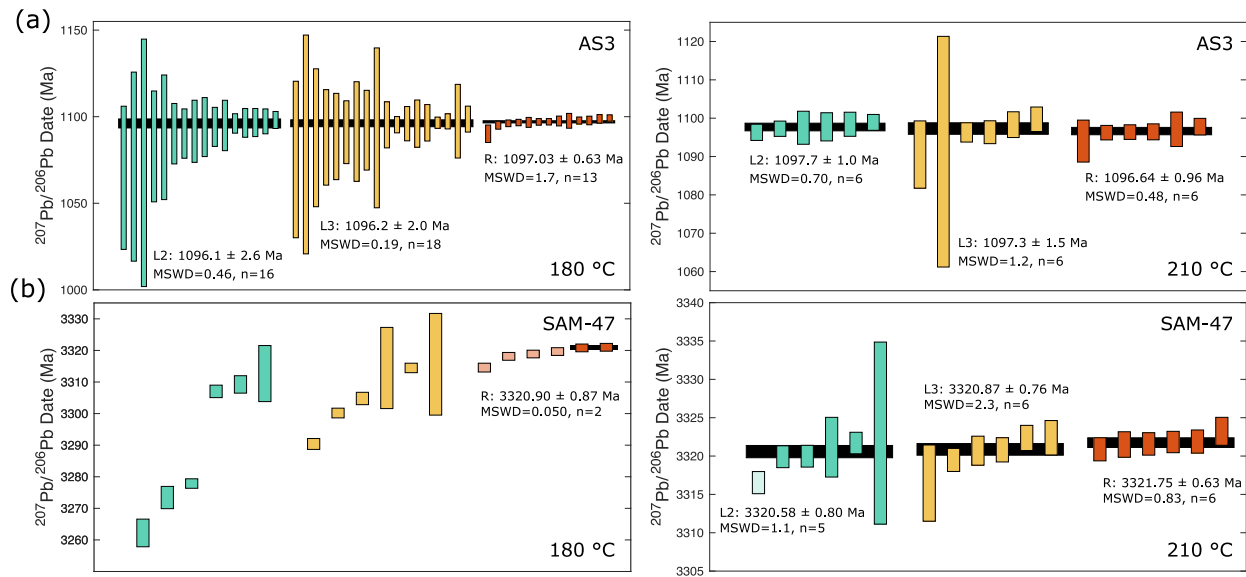
Figure 2. Ranked order ^{207}Pb/^{206}Pb dates for the **(a)** AS3 and **(b)** SAM-47 experiments. Black bars represent weighted means. Bar heights and quoted uncertainties reflect propagated 2σ analytical uncertainties.

951

952

953

954
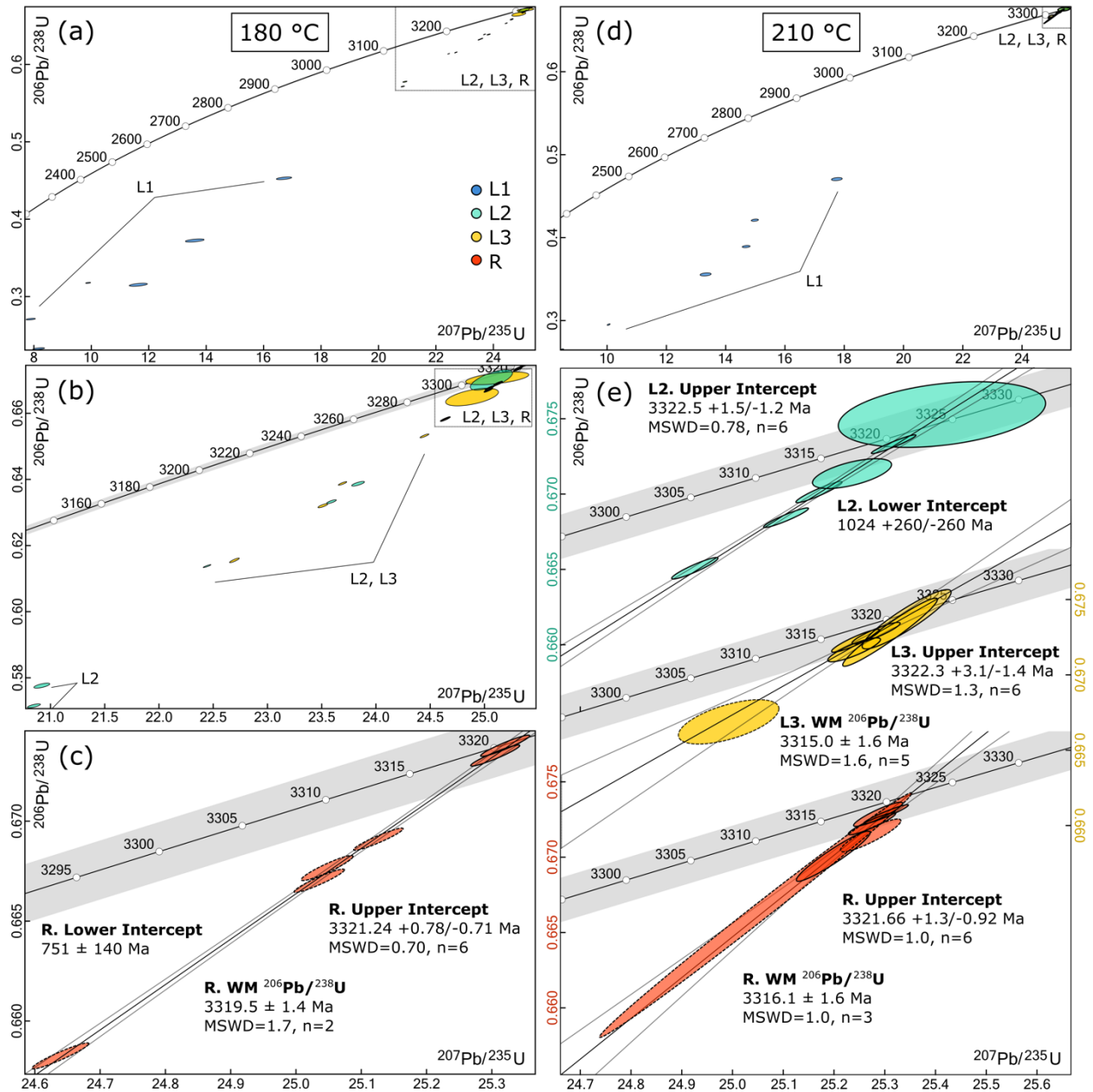
Figure 3. U-Pb concordia diagrams for the SAM-47 180 °C (left) and 210 °C (right) step-leaching experiments. **(a)** All data for the 180°C experiment. **(b)** Close up of the L2, L3, and R 180 °C dataset. **(c)** Close up of the 180 °C residue data. WM stands for weighted mean. **(d)** All data for the 210°C experiment. **(e)** Stacked plot showing the L2, L3, and R 210 °C datasets. All ellipses reflect 2σ analytical uncertainties. Dashed ellipses are excluded from weighted mean calculations.

955
956
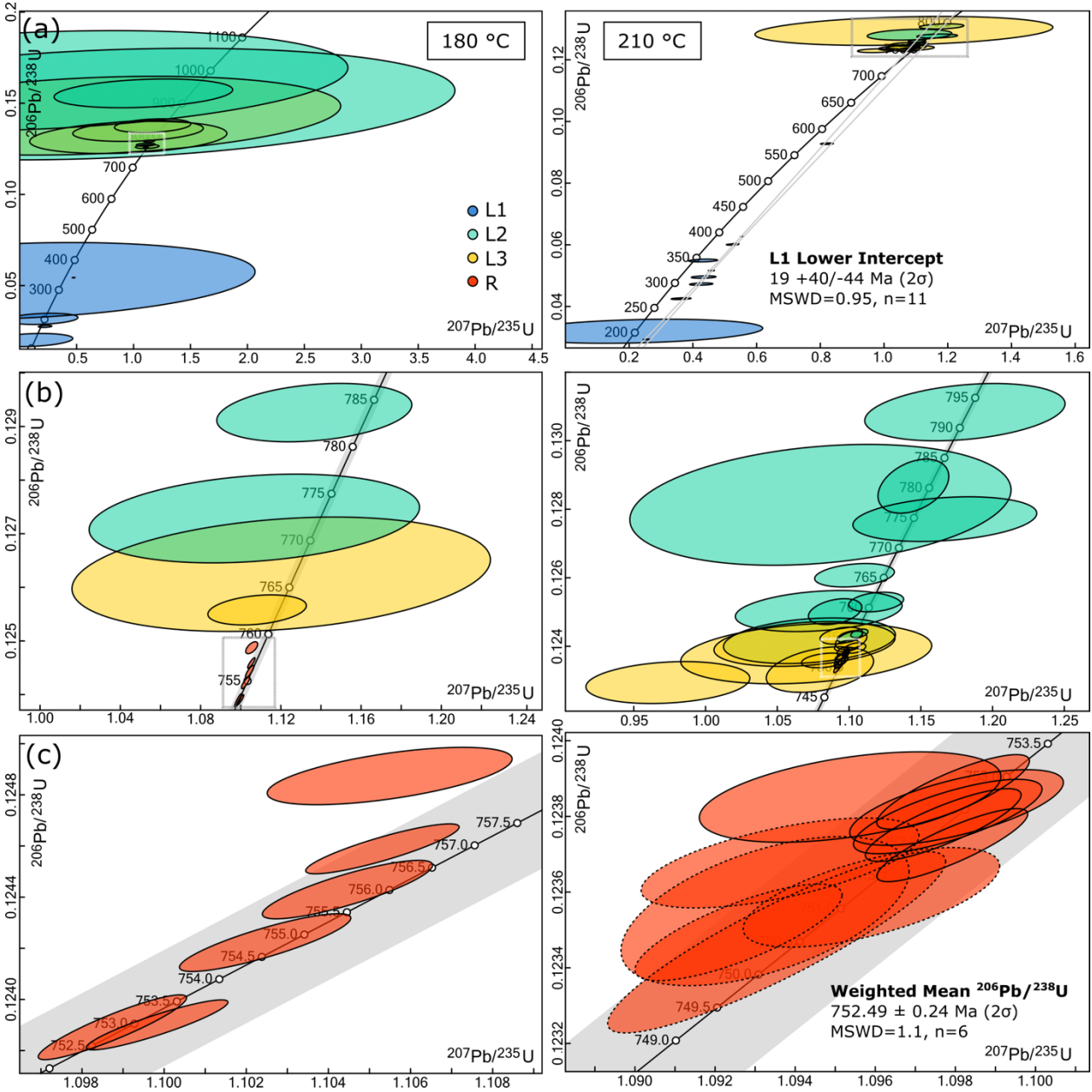
Figure 4. U-Pb concordia diagrams for the KR18-04 180 °C (left) and 210 °C (right) step-leaching experiments. **(a)** All data are depicted. **(b)** Close up of L2, L3, and R data excluding leachates with Pb*/Pb$_c$ values < 1. **(c)** Close up of zircon residues. The weighted mean ^{206}Pb/^{238}U date reported for the 210 °C experiment includes residue data with solid ellipse borders. Ellipses with dashed borders were excluded due to low-quality U measurements. All ellipses reflect 2σ analytical uncertainties.

957
958
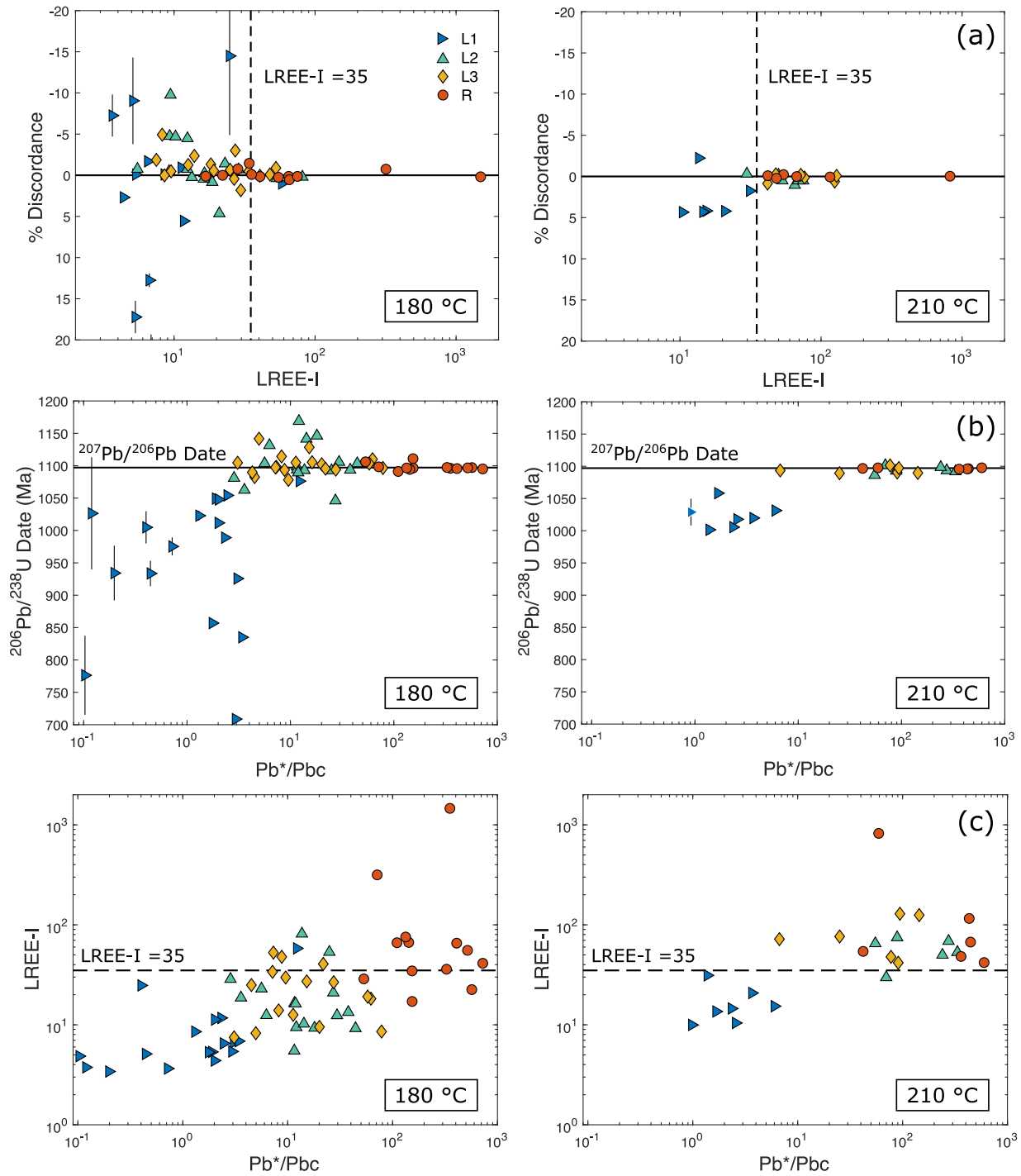
Figure 5. AS3 U-Pb and trace element data for the 180 °C (left) and 210 °C (right) experiments. **(a)** LREE-I versus percent discordance. The horizontal solid line represents perfect concordance. The vertical dashed line depicts a LREE-I threshold value of 35 below which data is notably more discordant. **(b)** ^{206}Pb/^{238}U date plotted as a function of the radiogenic Pb* to common Pb ratio. Error bars for the percent discordant and ^{206}Pb/^{238}U data reflect propagated 2σ analytical uncertainties. Most error bars are smaller than data markers. **(c)** The radiogenic Pb* to common Pb ratio versus the LREE-I showing a positive correlation between the two variables.

959
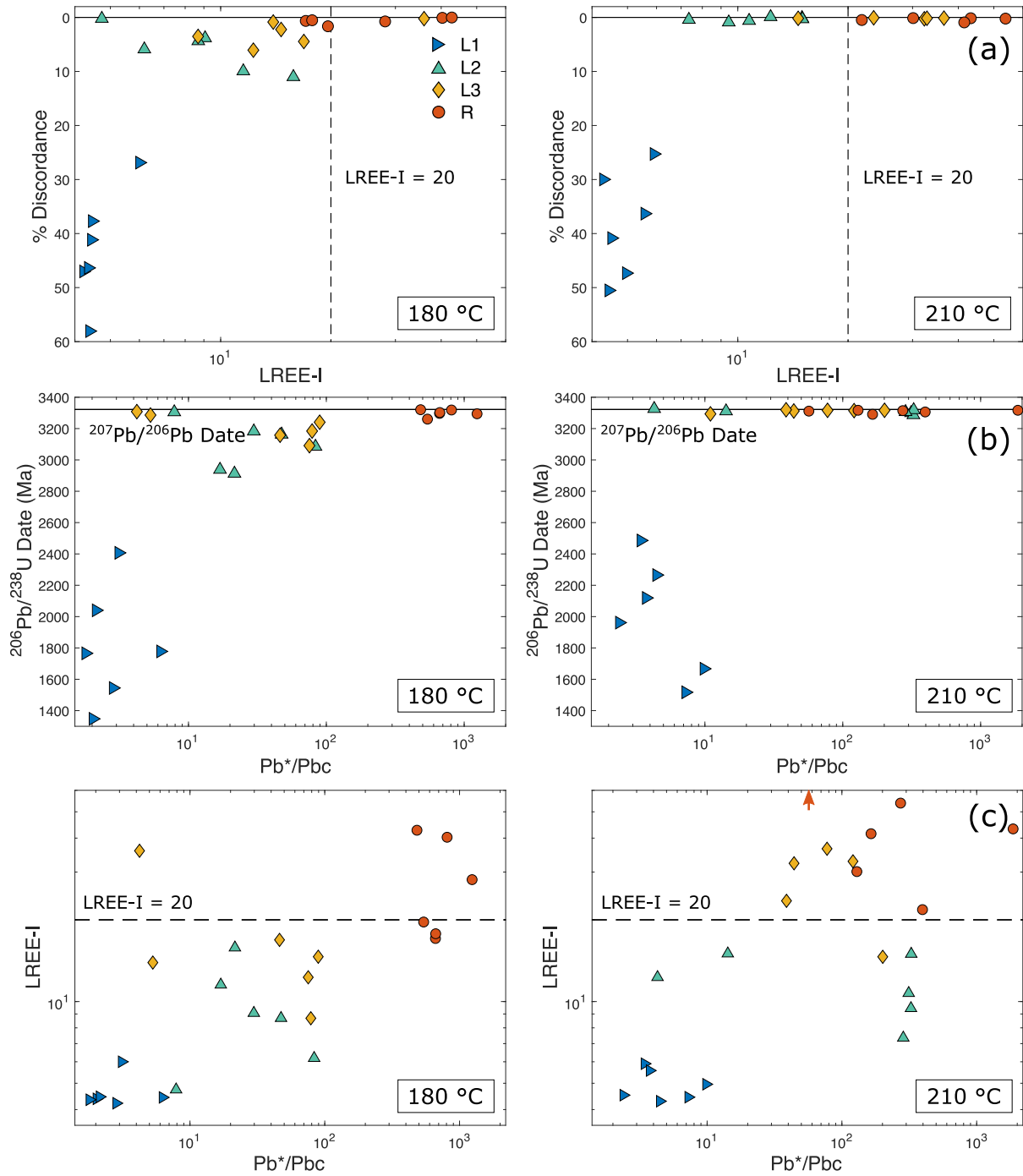
Figure 6. SAM-47 U-Pb and trace element data for the 180 °C (left) and 210 °C (right) experiments. **(a)** LREE-I versus percent discordance. The horizontal solid line represents perfect concordance. The vertical dashed line depicts a LREE-I threshold value of 20 below which data is notably more discordant. **(b)** ^{206}Pb/^{238}U date plotted as a function of the radiogenic Pb* to common Pb ratio. Error bars for the percent discordant and ^{206}Pb/^{238}U data reflect propagated 2σ analytical uncertainties. Most error bars are smaller than data markers. **(c)** The radiogenic Pb* to common Pb ratio versus the LREE-I showing a positive correlation between the two variables.

960
961
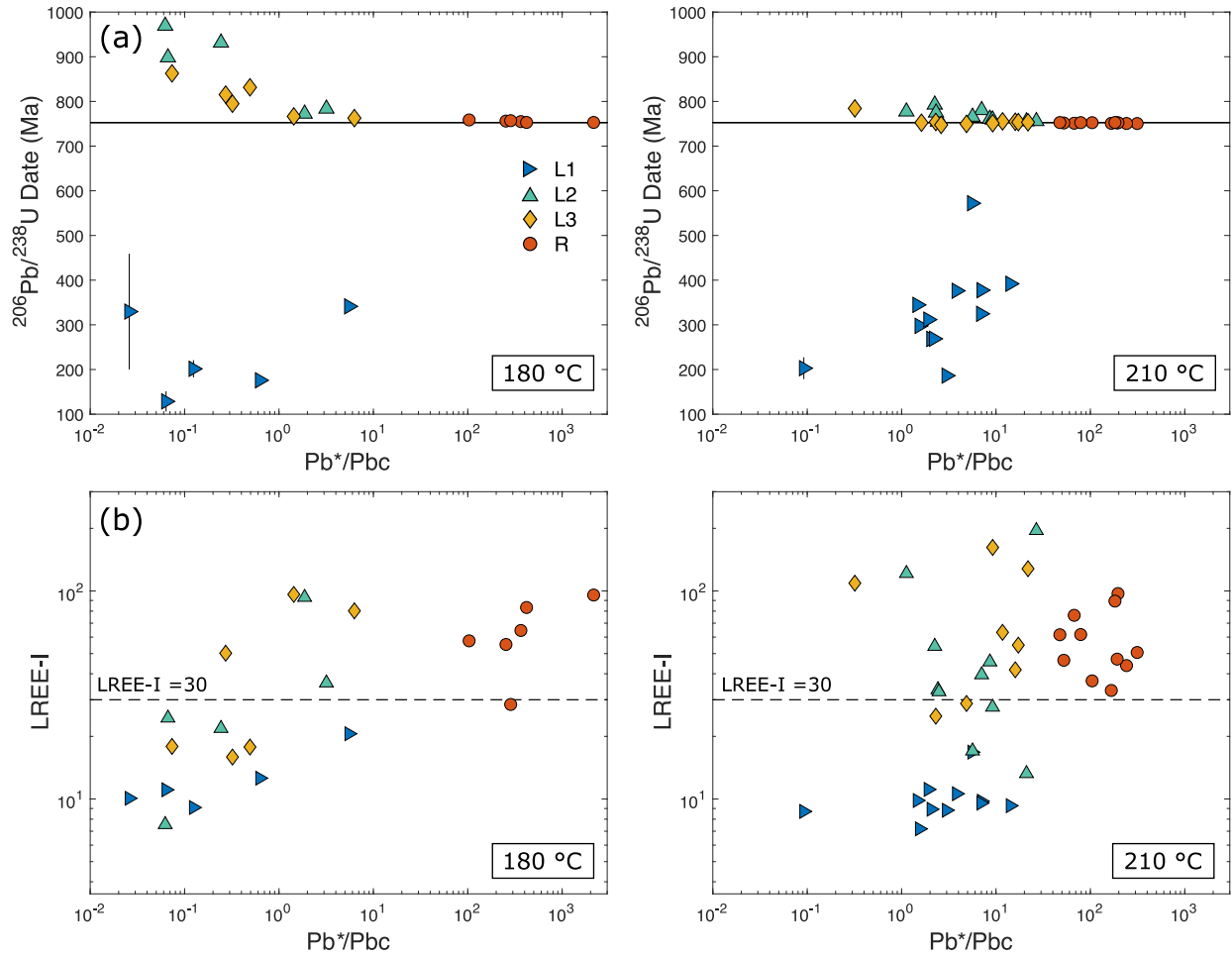
Figure 7. KR18-04 U-Pb and trace element data for the 180 °C (left) and 210 °C (right) experiments. **(a)** ^{206}Pb/^{238}U date plotted as a function of the radiogenic Pb* to common Pb ratio. 2σ analytical uncertainties for the percent discordant and ^{206}Pb/^{238}U data are smaller than data markers. **(b)** The radiogenic Pb* to common Pb ratio versus the LREE-I.

962
963
964
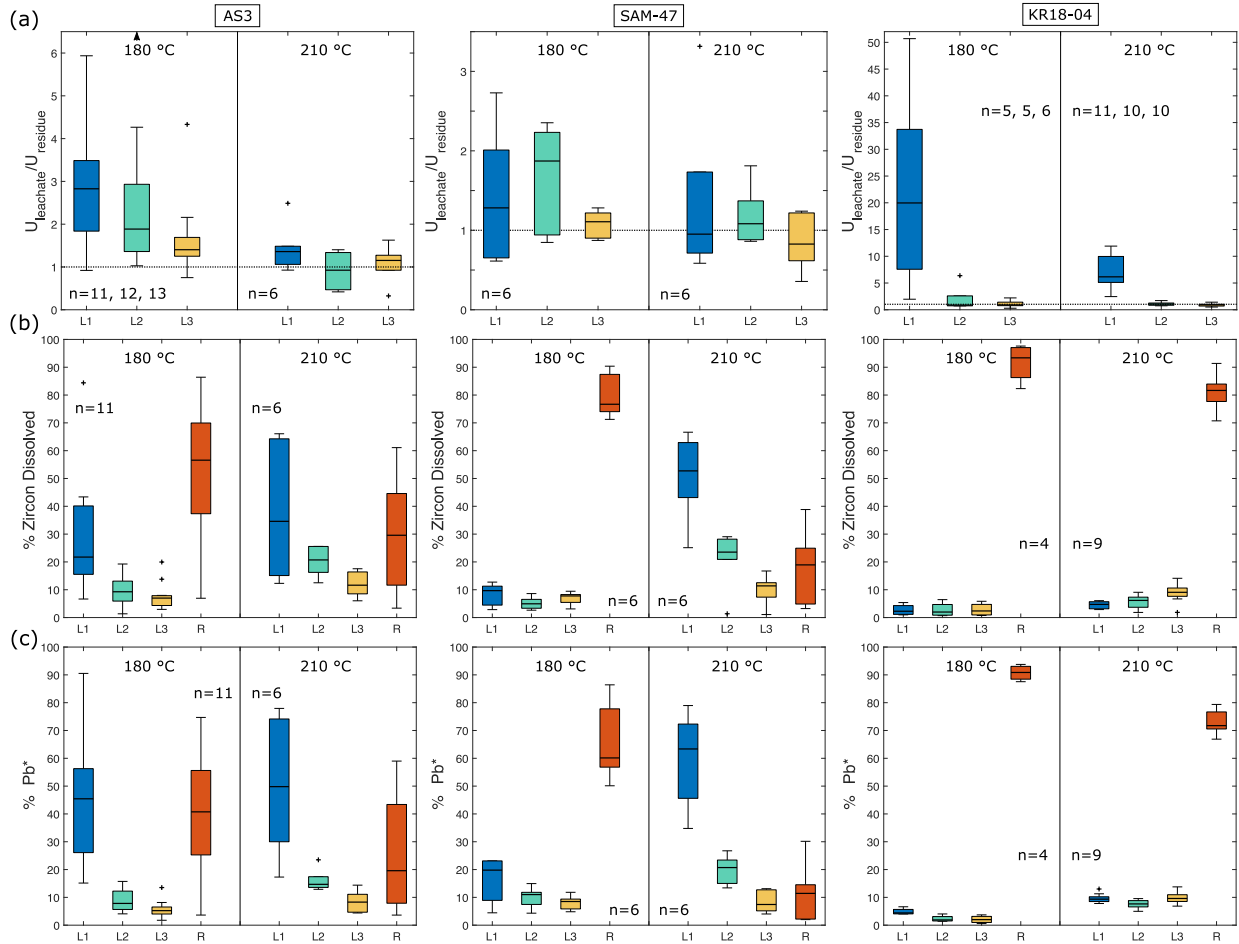
Figure 8. Box plot diagrams depicting geochemistry data for all step-leaching experiments. Each box shows the median value (black bar), the upper and lower quartiles (box), the minimum and maximum values (whiskers), and statistical outliers (plus marks) **(a)** Uranium concentration of leachates relative to that of their associated residue. **(b)** Percent zircon dissolved per leaching step based on measured Zr abundances. **(c)** Percent of radiogenic Pb measured per leaching step.

965
966
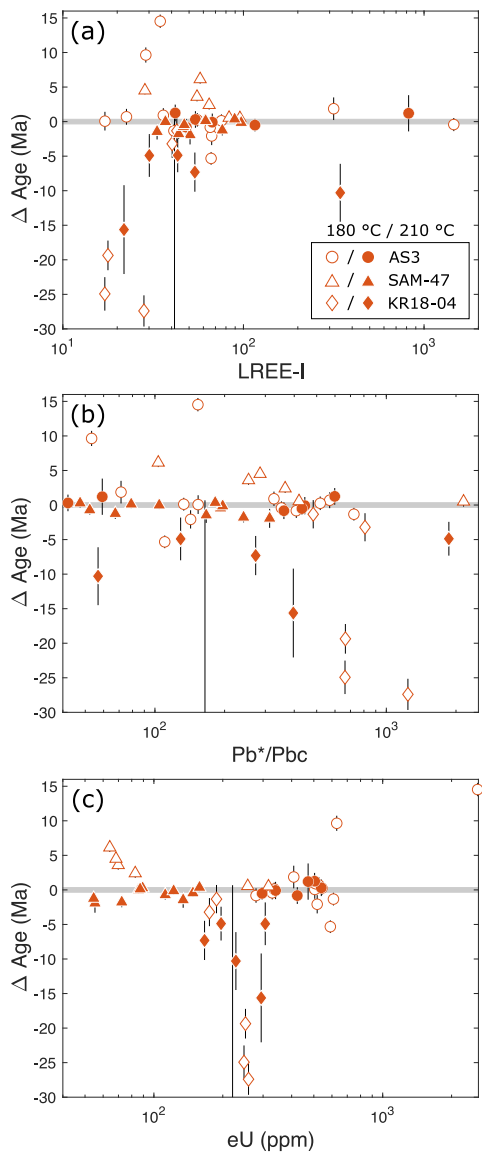
Figure 9. Trace element and Pb isotopic composition of zircon residues plotted against Δ Age as described in text. The gray bar at Δ Age = 0 Ma marks the accepted crystallization age for each zircon sample. **(a)** LREE-I versus the Δ Age. **(b)** Pb*/Pb$_c$ versus the Δ Age. **(c)** eU versus Δ Age. The arrow in each plot marks the placement of a datapoint from the SAM-47 dataset that plots at Δ Age = -60 Ma.

967
968
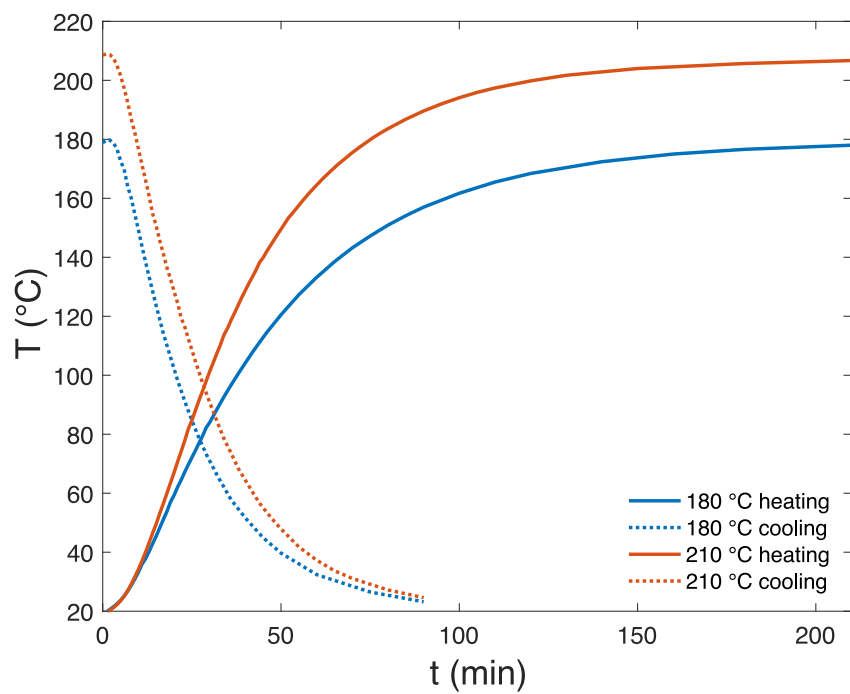
Figure 10. Temperature of the PTFE-lined pressure dissolution vessel plotted as a function of time. A fan was used to speed up cooling.

969
970
971
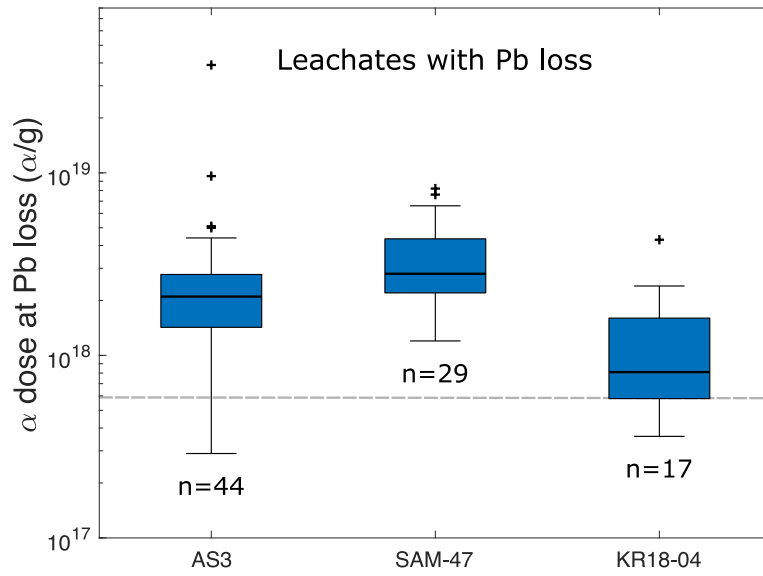
Figure 11. Box plot diagram showing alpha dose distribution for leachates (L1, L2, and L3) affected by Pb loss. Data include both the 180 °C and 210 °C experiments. The gray dashed line highlights our best estimate for the minimum alpha dose required for Pb loss to occur. Each box shows the median value (black bar), the upper and lower quartiles (box), the minimum and maximum values (whiskers), and statistical outliers (plus marks).

972
973
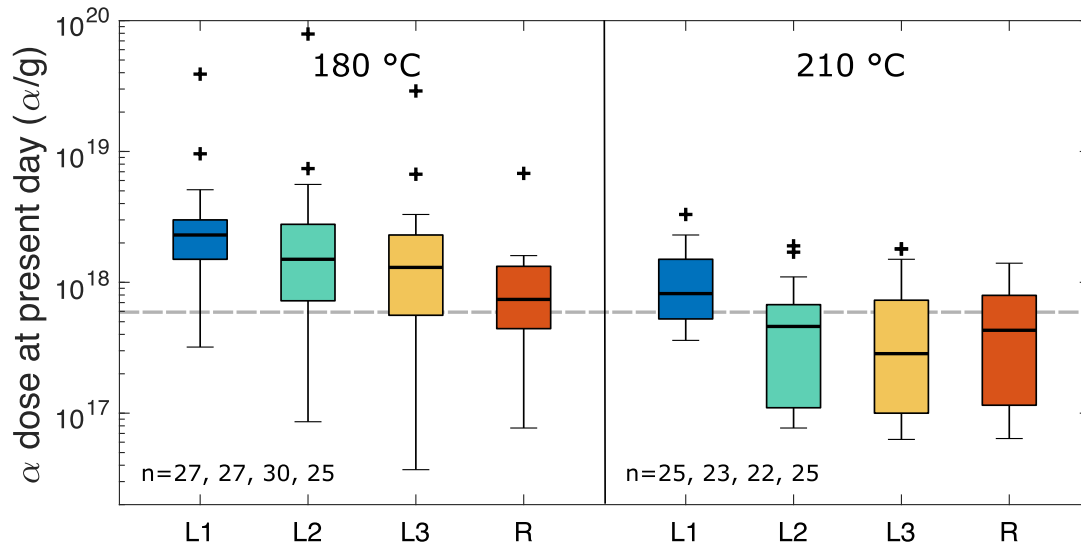
Figure 12. Box plot diagram showing present day alpha dose distributions at each step of zircon dissolution. Data includes all AS3, SAM-47 and KR18-04 leachates and residues. Alpha dose estimates reflect samples' present day radiation damage. The gray dashed line highlights our best estimate for the minimum alpha dose required for Pb loss to occur. Each box shows the median value (black bar), the upper and lower quartiles (box), the minimum and maximum values (whiskers), and statistical outliers (plus marks).

974
975
976
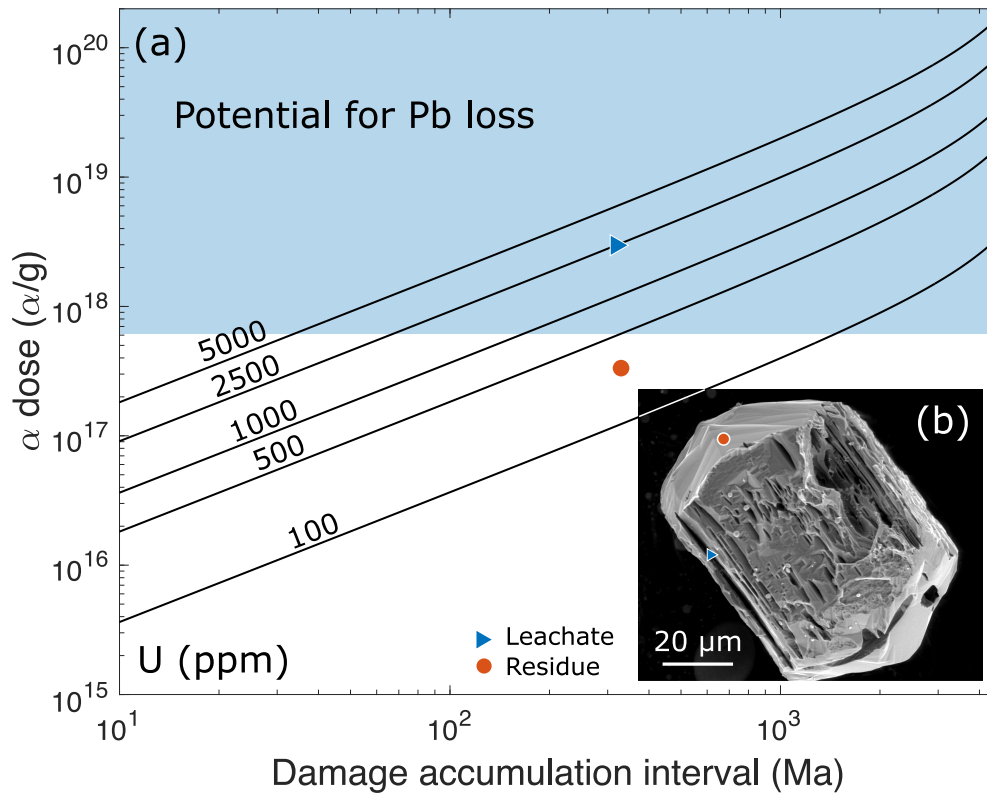
Figure 13. **(a)** Contour diagram showing alpha dose as a function of time for U concentrations ranging from 100 ppm to 5000 ppm. Calculations assume a fixed Th/U of 0.5 and no annealing. The shaded region highlights the alpha dose range in which Pb loss is most likely. **(b)** Secondary electron image of KR18-04 residue chemically abraded at 210 °C for 12 h from McKanna et al., (2023). The blue triangle marks a thin concentric zone that dissolved during chemical abrasion (leachate), while the red circle marks a portion of the zircon that remained intact (residue). Markers in b) correlate to markers in a) and illustrate how a grain with radionuclide zoning can have accumulated alpha doses above and below the threshold for Pb mobilization.

977
978
979

Table 1. Alpha dose estimates.

Sample	α dose (α/g)[1]						α_r dose (α/g)[2]	
	Total		Pb-Loss		Present Day		Present Day	
	Min	Max	Min	Max	Min	Max	Min	Max
AS3	4×10^{17}	1×10^{20}	3×10^{17}	8×10^{19}	3×10^{17}	8×10^{19}	2×10^{17}	$>1\times10^{19}$
SAM-47	2×10^{18}	1×10^{19}	1×10^{18}	8×10^{18}	3×10^{17}	2×10^{18}	6×10^{17}	2×10^{18}
KR18-04	1×10^{17}	1×10^{19}	4×10^{16}	4×10^{18}	4×10^{16}	4×10^{18}	5×10^{16}	7×10^{17}

[1]Calculated using measured U and Th concentrations and damage accumulation intervals as described in text.

[2]Raman-based alpha dose estimates reported by McKanna et al., (2023).

980